PCCP

ROYAL SOCIETY OF CHEMISTRY

PAPER

View Article Online
View Journal | View Issue

Cite this: *Phys. Chem. Chem. Phys.*, 2021, **23**, 23106

Reactive force fields for aqueous and interfacial magnesium carbonate formation†

Siavash Zare and Mohammad Javad Abdolhosseini Qomi *

Received 11th June 2021,
Accepted 29th September 2021

DOI: 10.1039/d1cp02627e

rsc.li/pccp

We develop Mg/C/O/H ReaxFF parameter sets for two environments: an aqueous force field for magnesium ions in solution and an interfacial force field for minerals and mineral–water interfaces. Since magnesium is highly ionic, we choose to fix the magnesium charge and model its interaction with C/O/H through Coulomb, Lennard-Jones, and Buckingham potentials. We parameterize the forcefields against several crystal structures, including brucite, magnesite, magnesia, magnesium hydride, and magnesium carbide, as well as Mg^{2+} water binding energies for the aqueous forcefield. Then, we test the forcefield for other magnesium-containing crystals, solvent separated and contact ion-pairs and single-molecule/multilayer water adsorption energies on mineral surfaces. We also apply the forcefield to the forsterite–water and brucite–water interface that contains a bicarbonate ion. We observe that a long-range proton transfer mechanism deprotonates the bicarbonate ion to carbonate at the interface. Free energy calculations show that carbonate can attach to the magnesium surface with an energy barrier of about 0.22 eV, consistent with the free energy required for aqueous Mg–CO_3 ion pairing. Also, the diffusion constant of the hydroxide ions in the water layers formed on the forsterite surface are shown to be anisotropic and heterogeneous. These findings can help explain the experimentally observed fast nucleation and growth of magnesite at low temperature at the mineral–water–CO_2 interface in water-poor conditions.

1. Introduction

Magnesium is an abundant alkaline-earth metal that plays a pivotal role in biological processes,[1] the automotive industry,[2] battery technology,[3] and mineral carbonation.[4] In particular, mineral carbonation in geological systems has gained considerable attention during the past two decades amid the record-high CO_2 concentration in the atmosphere. Carbonation is the reaction between CO_2 and Me^{2+}-containing minerals through natural weathering or geological sequestration that produces stable carbonate minerals. When dissolved in water, divalent metal cations like Mg^{2+} and Ca^{2+} bind to water molecules or negatively charged anions like carbonate anions. The pairing between magnesium/calcium and carbonate is a precursor for the precipitation of calcite ($CaCO_3$), dolomite ($CaMg(CO_3)_2$), and magnesite ($MgCO_3$), among other phases. However, the homogeneous nucleation and magnesite growth are slow at low temperatures (<80 °C) relevant to geological conditions. The sluggish magnesite precipitation could be in part the consequence of the higher water-binding energies of magnesium[5,6] or the lattice limitation of carbonate on the geometrical configuration of CO_3 groups in magnesite.[7]

Recently, magnesite precipitation was observed as the product of the reaction between synthetic and natural forsterite (Mg_2SiO_4), magnesium-rich end-member of olivine, and brucite ($Mg(OH)_2$) with water-saturated supercritical CO_2 and at low temperatures.[8–10] A common feature of all Me^{2+}-bearing minerals is that once they contact wet supercritical CO_2, a sub-nanometer water film forms on their surface that facilitate the formation of carbonic acid[11] and surface–metal complexes,[12,13] and if the thickness of water film is above a threshold, magnesite precipitation occurs.[14–16] Time-resolved quantitative X-ray diffraction (XRD) experiments coupled with molecular dynamics simulations show that four water layers are required to allow Mg ion diffusivity across the water layers, enabling high rates of magnesite precipitation.[16] Also, *in operando* XRD experiments on the surface of forsterite in contact with wet supercritical CO_2 at various temperatures revealed an anomalously low activation energy barrier for the formation magnesite.[17] However, the underlying molecular mechanism of the carbonation reaction at the sub-nanometer olivine–water–CO_2 interface is puzzling due to experimental spatiotemporal limitations.[12,18,19]

Indirect observations suggest that the lower dehydration energy of magnesium in the adsorbed water film is due to the presence of organic ligands[20,21] dissolved in CO_2 or the

Department of Civil and Environmental Engineering, University of California, Irvine, CA, USA. E-mail: mjaq@uci.edu

† Electronic supplementary information (ESI) available. See DOI: 10.1039/d1cp02627e

calcium-like water coordination shell of Mg^{2+} in the adsorbed water nanofilm.[17] However, the exact mechanism remains unknown. Molecular simulations promise to address this knowledge gap by providing an atomic-level insight into the physicochemical nature of the carbonation reaction at the olivine–water–CO_2 interface. First principle calculations offer promising avenues to explore chemical reactions at the nanoscale. For instance, quantum mechanical calculations indicate the H_2O exchange promotes the dissolution of Mg-/Ca-silicate clusters.[22] *Ab initio* thermodynamics simulations also show the partial hydroxylation of the most active forsterite surface cleavages when in contact with two monolayers of water at geologically relevant temperatures.[23]

However, such quantum mechanical calculations become exorbitantly expensive when the number of atoms exceeds a few hundred. Furthermore, the dynamics of interfacial and bulk water are still not captured without uncertainty in these calculations due to complications in capturing dispersion effects. Force field (FF) methods can potentially address these issues and delve into the atomistic-level details reaching microseconds. Classical molecular dynamics (MD) simulations show that water adsorption on the forsterite surface is exothermic even at undersaturated high CO_2 pressures. They also confirm that CO_2 is displaced from the (010) forsterite surface by the adsorbed water molecules except at low water coverages.[24] Raiteri *et al.*[25] have successfully developed a thermodynamically stable FF to model magnesium–(bi)carbonate ion pairing in the solution. Nevertheless, the current FFs for interfacial and bulk magnesium carbonate formation are nonreactive, *i.e.*, they cannot simulate proton transfer processes and interfacial chemical reactions. Here, we attempt to develop a reactive FF to model carbonation reactions in bulk water and at the interface of magnesium-containing silicates and hydroxides.

This paper extends the current ReaxFF potential library to include magnesium interactions with oxygen, hydrogen, and carbon in an aqueous, bulk, and interfacial environment. The charge of magnesium is kept fixed, although the charge equilibration scheme in ReaxFF operates as usual for the rest of the elements. The geometrical and mechanical properties of a wide range of magnesium-containing crystals and magnesium–water binding energies are taken as observables in the fitting process. After completing the parameterization stage, we test the resulting parameters for reproducing a group of magnesium-containing solids, water adsorption on crystal surfaces, and Mg–(H)CO_3 ion pairing in the solution. Then, we explore our FF for some reactive environments, including the proton transfer between bicarbonate and brucite surface, the free energy calculation of the adsorption of carbonate on the forsterite surface, and carbonic acid dissociation in water in the presence of magnesium ion.

2. Methods

To describe molecular interactions in magnesium carbonate systems, we derive and validate a set of potential parameters and merge the results with a previously-fitted ReaxFF forcefield[26] that was applicable to aqueous and interfacial calcium carbonate systems. ReaxFF is a bond-order-based FF that can simulate covalent bond formation and breakage. It also implements a charge equilibration scheme that calculates atomic charges based on geometry and electronegativity.[27] The total potential energy, E_{tot}, in ReaxFF is written as:

$$E_{tot} = E_{bond} + E_{vdW} + E_{qeq} + E_{pen} + E_{over} + E_{under} + E_{val} + E_{tors} + E_{conj} \quad (1)$$

where E_{bond}, E_{vdW}, E_{qeq}, E_{pen}, E_{over}, E_{under}, E_{val}, E_{tors}, and E_{conj} are respectively bonded, van der Waals, coulombic, penalty, over-coordination, under-coordination, valence angle, torsion, and conjugation energies. Like calcium, magnesium is present primarily as di-cation due to its ionic nature, except for the case of shortly-lived univalent Mg^{+} observed in the corrosion of magnesium alloys.[28] This allows us to incorporate a fixed magnesium charge and follow the recipe for the fitting of ReaxFF for calcium carbonate systems that treat calcium charge fixed without any bond-order consideration. To model electrostatics, we use the screened Coulomb potential between atom i and j, as implemented in REAXFF:[7]

$$E_{coulomb} = \mathrm{Tap} \cdot C \cdot \frac{q_i q_j}{\left[r_{ij}^3 + \left(1/\gamma_{ij}\right)^3\right]^{1/3}} \quad (2)$$

where q_i and q_j are the charges of atoms i and j respectively, Tap is a 7th order polynomial taper function that depends on the distance between the two atoms. This taper function ensures that coulombic energy does not have discontinuity when charges enter or leave the cutoff radius of 10 Å. γ_{ij} is the pairwise screening parameter derived from the geometric mean of single atom screening parameters γ_i and γ_j.

For the short-range repulsive Mg–C and Mg–H interactions, we choose the repulsive portion of the Buckingham potential as follows:

$$E_{ij} = A_{ij} e^{-r_{ij}/\rho_{ij}} \quad (3)$$

where A_{ij} and ρ_{ij} are characteristic energy and length, respectively. We also choose 12-6 Lennard-Jones (LJ) potential for Mg–O interaction:

$$E_{ij} = \frac{A_{ij}}{r^{12}} - \frac{B_{ij}}{r^6} \quad (4)$$

where A_{ij} and B_{ij} are LJ fitting parameters. We note that in the reactive FF developed for the calcium carbonate systems,[26] only the repulsive part of the Lennard-Jones (12-6) potential was chosen to describe the short-range interaction for Ca–O pairs based on the realistic assumption that Ca^{2+} have negligibly small electronic polarizability. However, in our fitting process, the attractive part of the Lennard-Jones potential for Mg–O interactions helps achieve accurate magnesium hydration energies and magnesium–water distance.

Atomic point charges are usually fixed in most classical MD frameworks, and therefore the effect of the environment on the distribution of charges is neglected. However, in ReaxFF, a similar approach to electronegativity equalization method (EEM) is used

to update atomic charges at every step based on the geometry and fitted atomic properties.[29–32] In this method, total electrostatic energy comprised of intra-atomic and interatomic potentials is defined as:

$$E_{\mathrm{es}}(q_1 \ldots q_N, x_1 \ldots x_N) = \sum_i \left(E_{i0} + \chi_i q_i + \frac{1}{2} J_i q_i^2 \right) + \sum_i \sum_{j<i} q_i q_j J_{ij} \quad (5)$$

where x_i is the location of atom i, q_i is its charge, E_{i0} is a zeroth-order constant, χ_i is the electronegativity, J_i is the self-coulomb repulsion in atom i, and J_{ij} is the Coloumb potential between two unit charges located at x_i and x_j. The self-coulomb potential could be understood as the electrostatic repulsion between two electrons in a doubly-occupied orbital. The first sum represents the Taylor series expansion of the energy of an isolated atom up to the second order. The second sum represents the conventional inter-atomic Coulomb potential between atoms i and j that is inversely proportional to their distance, $|x_i - x_j|^{-1}$.

The equilibrium charge distribution is achieved when the first derivatives of the total potential with respect to each charge, $\frac{\partial E_{\mathrm{es}}}{\partial q_i}$ or chemical potentials, are all equal. Applying the constraint that the total charge of the system is constant and using the Lagrange multiplier method leads to the following linear equation:

$$\sum_j M_{ij} q_j = \mu - \chi_i \quad (6)$$

where M_{ij} and μ are respectively the coulomb-interaction matrix and the Lagrange's multiplier. If some charges are fixed in the system, it is only required to construct the above matrix equation for variable charges q_i while subtracting the inter-atomic Coulomb potential between the fixed charges and unit charges at location x_i on the right-hand side.

To fit the FF parameters, namely Mg–C, Mg–H, Mg–O and γ_{Mg} potential parameters, we employ the iterative fitting scheme that was previously used to fit the parameters of fixed-charge-calcium REAXFF.[26] To this end, we minimize the error function defined as the sum of squares of the difference between experimental/DFT observable value and ReaxFF-calculated value:

$$F = \sum_{i=1}^{N} w_i \left(f_i^{\mathrm{obs}} - f_i^{\mathrm{calc}} \right)^2 \quad (7)$$

where f_i^{obs} is the experimental/DFT-derived quantity, f_i^{calc} is the ReaxFF-calculated quantity, w_i is the weighting factor for the given quantity, and N is the number of observables. The selected observables are the solid lattice constants, atomic configurations, bond/angle values, and bulk modulus for some of the crystals selected for fitting, as shown in Table 1.

In each iteration, first the Mg–H and Mg–C parameters are fitted to the lattice structure of αMgH_2,[33] and MgC_2[34] and the bulk modulus of αMgH_2. Then, the derived Mg–H and Mg–C parameters are used to fit Mg–O and γ_{Mg} using the lattice structure and the bulk modulus of $Mg(OH)_2$,[35,36] MgO,[37] and $MgCO_3$[38,39] crystals along with the total hydration energies (E_{hyd}) of water molecules on the first and second shell[40] of Mg^{2+}, namely $[Mg(H_2O)_6]^{2+}$ and $[Mg(H_2O)_6](H_2O)^{2+}$. Note that the Mg–H and Mg–C parameters are kept fixed at this step. Also, the Mg–Ow bond length of the first shell of water molecules and some of the Mg–Ow–Ow angles were taken as fitting observables, in which Ow being the oxygen in the water in the first and second shell. We repeat these two steps iteratively until we obtain a satisfactory parameter set.

Based on water adsorption calculation on crystal surfaces described later, assigning a formal charge of +2 to magnesium atoms causes an overestimation of water adsorption energies compared to density functional theory (DFT) calculations. Since electrostatics contributions play a significant role in water adsorption energies on crystal surfaces, we decided to parameterize two separate force fields: (1) the aqueous FF with magnesium charge fixed to +2, which is suitable for aqueous magnesium carbonate systems, and (2) the interfacial FF, for which we fit the magnesium charge to the geometrical and mechanical properties of magnesium-containing solids and can be used for crystalline solids and their interfaces with water. Note that we only used the Mg–water cluster to fit the aqueous FF and not the interfacial FF. Also, the charge of magnesium in the interfacial FF is fitted in the second step of each iteration.

Magnesium–water clusters are simulated using the Gaussian16 code.[41] B3LYP exchange–correlation functional[42,43] is used with the large 6-311++G(2d,2p) basis set. Berny optimization method[44] is used with the Tight option and Ultrafine integration grid[45] to ensure convergency is reached for clusters with soft degrees of freedom. Dispersion correction is applied using the DFT-D3 method of Grimme.[46,47]

Table 1 The training dataset for parameterization of the forcefield. MgC_2, MgH_2, MgO, $MgCO_3$, and $Mg(OH)_2$ are crystal structures. $Mg^{2+}[H_2O]_6$ and $Mg^{2+}[H_2O]_6[H_2O]_2$ are magnesium–water clusters consisting first and second shell of waters, respectively. Magnesium–water clusters are only used to fit the aqueous forcefield, while crystal structures are used for both aqueous and interfacial forcefields. The Mg–O–O angles are the angles between water and magnesium in the first and second hydration shells

Structure	Lattice constants	Atomic configuration	Bulk modulus	Bond distance	Angle value	Hydration energy
MgC_2	×	×				
MgH_2	×	×	×			
MgO	×	×	×			
$MgCO_3$	×	×	×			
$Mg(OH)_2$	×	×	×			
$Mg^{2+}[H_2O]_6$				Mg–Ow	Mg–Ow–Ow	×
$Mg^{2+}[H_2O]_6[H_2O]_2$				Mg–Ow	Mg–Ow–Ow	×

To calculate surface hydration energies, we implement Vienna Ab-initio Simulation Package (VASP).[48] Projector augmented wave (PAW) potentials[49] are used with the kinetic cut-off energy of 520 eV. The Perdew–Burke–Ernzerhof (PBE) generalized gradient approximation (GGA) is used as the exchange–correlation functional.[50] Also, van-der-Waals dispersion forces are considered using the DFT-D3 method of Grimme. For the crystal surfaces, $2 \times 2 \times 1$ mesh points are used to sample the *K*-space using Monkhorst–Pack scheme. Conjugate gradient method is used for geometry optimization. For simplicity, we refer to the DFT methods used for cluster and surface calculations as B3LYP-D3 and PBE-D3 respectively.

3. Results and discussions

3.1 Solvation structures and energies

The final fitted parameters derived according to the procedure described in the Methods section are presented in Table 2. These parameters should accompany the ReaxFF library provided in the ESI.† The hydration energies of magnesium are calculated for clusters up to eight water molecules, as shown in Table 3 and Fig. 1. The total hydration energy, E_{hyd}, the binding energy, E_{bind}, and the difference in the energies if one water molecule was added to the cluster, E, are calculated based on the following relationships:

$$E_{hyd} = E\{Mg(H_2O)_n{}^{2+}\} - E\{(H_2O)_n\} - E\{(Mg^{2+})\} \quad (8)$$

$$E_{bind} = E\{Mg(H_2O)_n{}^{2+}\} - nE\{(H_2O\} - E\{(Mg^{2+})\} \quad (9)$$

$$\Delta E = E\{Mg(H_2O)_n{}^{2+}\} - E(H_2O) - E\{Mg(H_2O)_{n-1}{}^{2+}\} \quad (10)$$

The difference between total hydration energy and binding energy is that the energy of a cluster of water molecules is used in the hydration energy while the energy of a single water molecule is used in the calculation of binding energies. The dispersion correction used in our B3LYP-D3 calculations can affect the water cluster energies. The magnitude of the binding energies (E_{bind}) calculated from our B3LYP-D3 calculations are larger than those previously calculated from B3LYP calculations[5] without dispersion corrections. The discrepancy in binding energies is expected when we use dispersion correction that was shown to more accurately capture van der Waals interactions and hydrogen bonding.[51–53] $|E|$ reduces as the number of water molecules increases in ReaxFF and DFT. Also, as the number of water molecules increases, the error in ReaxFF hydration energies compared to DFT results reduces. This is due in parts to the charge equalization scheme in ReaxFF that tends to uniformly distribute charges, therefore working better for larger clusters where charges are less localized.

We also provide in Table 3 the binding energies resulted from two known non-reactive potentials. One is the core–shell potential developed by Kerisit and Parker,[54] which is successfully used to study the free energy of metal cation (Sr, Mg, Ca) adsorption on the surface of calcium carbonate crystal. The other is the thermodynamically consistent forcefield developed by Raiteri *et al.*[25] to model alkaline-earth carbonates in water.

As reported in Table 3, our reactive forcefield gives more accurate results than both non-reactive forcefields for the binding energies of clusters with equal or more than 4 water molecules. This roots back in the charge equalization method implemented in our forcefield that does not perform accurately for localized charges, whereas for the systems with more distributed charges it is shown to be more reliable. The energy difference in binding energies (ΔE) are captured well through both reactive and the non-reactive forcefields especially when we add water molecules to the first shell of magnesium. When we add water to the second shell, although binding energies calculated from our reactive forcefield are within a good range of binding energies calculated from DFT-D3, we observe larger discrepancy in ΔE. This can be the result of limited charge screening in our forcefield due to the fixed magnesium charge. Same is true for the Raiteri *et al.*'s forcefield with fixed charges, whereas the Kerisit and Parker's forcefield is more consistent in calculating ΔE, due to the polarizability of water molecules provided by the core–shell model. Also, we report the hydration and binding energies of magnesium–water cluster calculated from our interfacial forcefield in Table 3. As shown in the table, the interfacial reactive forcefield gives much less accurate results when compared to the aqueous ReaxFF due to the smaller Mg charge.

The distance between Mg^{2+} and water oxygens in $Mg(H_2O)_n{}^{2+}$ as obtained from ReaxFF, our DFT simulations, and a previous DFT work[5] are presented in Table 4. Our B3LYP-D3 calculations show slightly larger bond lengths between magnesium and the water oxygens compared to previous B3LYP calculations. Similar overestimations were observed for the Na^+–water bond lengths when dispersion correction was implemented.[55] On the other hand, ReaxFF gives acceptable bond distance values, although in general overestimates them. The Mg–Ow bond lengths increase as the number of water molecules increases, in agreement with DFT results.

Table 2 Fitted interatomic potential parameters to be incorporated with REAXFF. The Mg–H and Mg–C interactions are modelled with Buckingham potential (eqn (3)) and the Mg–O interaction is modelled with Lennard-Jones (LJ) 12-6 potential (eqn (4)). Gamma is the screening parameter used in Coulombic interaction according to eqn (2)

	Aqueuos forcefield						Interfacial forcefield					
Interaction	q_{Mg}	γ (Å^{-1})	A_{lj} (eV Å^{12})	B_{lj} (eV Å^6)	A_{buck} (eV)	ρ_{buck} (Å)	q_{Mg}	γ (Å^{-1})	A_{lj} (eV Å^{12})	B_{lj}(ev Å^6)	A_{buck} (eV)	ρ_{buck} (Å)
Mg Coulomb	2.00	0.55	—	—	—	—	1.2846	0.5298	—	—	—	—
Mg–H	—	—	—	—	293.366	0.289894	—	—	—	—	246.154	0.2572
Mg–C	—	—	—	—	320.9	0.37	—	—	—	—	240.6954	0.3228
Mg–O	—	—	3704.1911	44.480255	—	—	—	—	3646.7034	53.5115	—	—

Table 3 Water binding energies (eV) calculated for $[Mg(H_2O)_n](H_2O)_m^{2+}$. n and m refer to the number of water molecules in the first and second shell respectively. Hydration energy (E_{hyd}), binding energy (E_{bind}), and successive (ΔE) binding energy are calculated based on eqn (8)–(10), respectively

Cluster	E_{hyd} ReaxFF(aq) (eV)	E_{bind} ReaxFF(aq) (eV)	ΔE ReaxFF(aq) (eV)	E_{hyd} ReaxFF(int) (eV)	E_{bind} ReaxFF(int) (eV)	ΔE ReaxFF (int) (eV)	E_{hyd} B3LYP-D3 (eV)	E_{bind} B3LYP-D3 (eV)	ΔE B3LYP-D3 (eV)	E_{bind} B3LYP[a] (eV)	ΔE B3LYP[a] (eV)	E_{bind} non-reactive FF (eV)	ΔE non-reactive FF (eV)
$n = 2, m = 0$	−5.42	−5.67		−3.21	−3.47		−6.59	−6.83		−6.61		−4.76[d], −5.95[e]	
$n = 3, m = 0$	−7.49	−8.08	−2.41	−4.33	−4.92	−1.45	−8.66	−9.43	−2.59	−9.00	−2.39	−6.93[d], −8.15[e]	−2.17[d], −2.77[e]
$n = 4, m = 0$	−9.47	−10.15	−2.07	−5.43	−6.13	−1.21	−10.47	−11.53	−2.11	−10.90	−1.90	−8.92[d], −9.97[e]	−1.98[d], −2.44[e]
$n = 5, m = 0$	−10.15	−11.57	−1.41	−5.43	−6.84	−0.71	−11.29	−13.02	−1.49	−12.11	−1.21	−10.34[d], −11.2[e]	−1.42[d], −1.57[e]
$n = 6, m = 0$	−10.98	−12.84	−1.27	−5.60	−7.46	−0.62	−12.10	−14.39	−1.37	−13.18	−1.06	−11.77[d], −12.22[e]	−1.43[d], −1.52[e]
$n = 6, m = 1$[b]	−11.68	−14.05	−1.21	−6.51	−8.03	−0.56	−12.55	−15.32	−0.92	−13.96	−0.78		
$n = 6, m = 1$[c]	−11.64	−14.01	−1.17	−6.60	−8.12	−0.65	−12.62	−15.38	−0.98	−14.00	−0.82	−12.6[d], −12.64[e]	−0.83[d], −0.93[e]
$n = 6, m = 2$	−12.09	−15.03	−1.02	−5.80	−8.74	−0.62	−13.21	−16.22	−0.84	−14.62	−0.66	−13.31[d], −12.93[e]	−0.71[d], −1.06[e]

[a] From ref. 39. [b] One hydrogen bond. [c] Two hydrogen bonds. [d] Core–shell potential.[24] [e] Thermodynamically consistent potential.[25] (aq) refers to aqueous and (int) refers to interfacial forcefields.

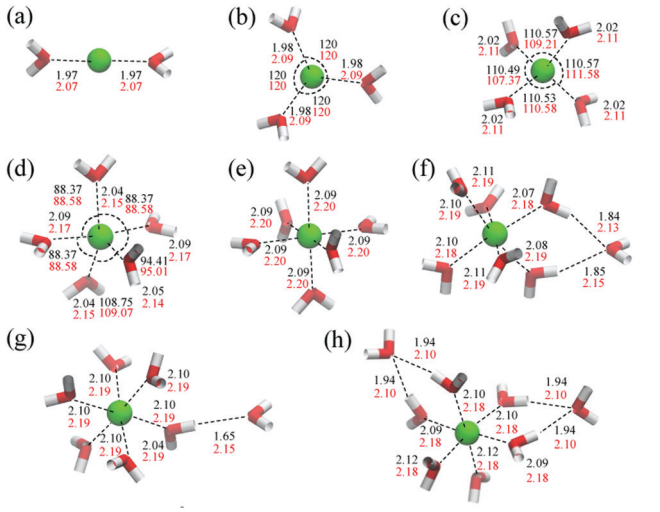

Fig. 1 Mg^{2+}–Water clusters. (a) $Mg^{2+}(H_2O)_2$ (b) $Mg^{2+}(H_2O)_3$ (c) $Mg^{2+}(H_2O)_4$ (d) $Mg^{2+}(H_2O)_5$ (e) $Mg^{2+}(H_2O)_6$ (f) $Mg^{2+}(H_2O)_6(H_2O)$. The water molecule in the second shell has one hydrogen bond with a first-shell water molecule (g) Mg^{2+}–$(H_2O)_6(H_2O)$. The water molecule in the second shell has two hydrogen bonds with two first-shell water molecules (h) Mg^{2+}–$(H_2O)_6(H_2O)_2$. The black and red values respectively refer to B3LYP-D3 and ReaxFF calculations. Mg atoms are shown by green balls, and water oxygen and hydrogen atoms are colored as red and white sticks, respectively.

Table 4 Bond distances between Mg^{2+} and water oxygen derived from ReaxFF and DFT in $[Mg(H_2O)_n]^{2+}$ clusters

Cluster	Mg–Ow (Å) ReaxFF	Mg–Ow (Å) B3LYP-D3	Mg–Ow (Å) B3LYP[a]
$n = 2$	2.07	1.95	1.95
$n = 3$	2.09	1.97	1.97
$n = 4$	2.11	2.02	1.99
$n = 5$	2.15, 2.17	2.04, 2.09	2.03, 2.07
$n = 6$	2.20	2.09	2.08

[a] From ref. 39.

3.2 Crystal structures

The resulting fitted parameters are used to calculate the lattice properties and bulk moduli of a list of magnesium-containing solid phases, as shown in Table 5. Along with the crystals used in the fitting procedure, few other crystal structures are selected to evaluate the transferability of the derived FF beyond the geometrical and mechanical observables used in the parameterization process. Here, we present the calculated crystal structures based on both aqueous and interfacial FF to show the impact of setting magnesium charge to a value less than +2 as expected for covalent-ionic systems.

As shown in Table 5, magnesite lattice parameters are reproduced with acceptable accuracy with both forcefields compared to experimental results. However, the bulk modulus is best captured with the interfacial FF with an underestimation of about 9%, while the aqueous FF produces poor results. The elastic constant, C_11, is calculated to be 168 GPa for magnesite according to our interfacial FF, which is reasonable compared to DFT calculations with GGA functional. However, it deviates

Table 5 Lattice properties and bulk modulus for magnesium containing crystals calculated from two fitted ReaxFF forcefields, compared to experiments

	Aqueous forcefield			Interfacial forcefield					
Crystal formula	a (Å)	c (Å)	K (GPa)	a (Å)	c (Å)	K (GPa)	a (Å)- exp.	c (Å)- exp.	K (GPa)- exp
Brucite	12.17	14.42	60	12.35	12.85	73	12.57	14.3	46
Magnesia	8.62			8.96			8.94		
Magnesite	5.94	17.83	163	6.11	18.36	105.18	5.67	17.02	110
Magnesium hydride	18.69	15.25	58.8	18.69	15.77	21	17.94	15	51
Magnesium carbide	16.78	15.71		17.22	14.92		15.74	15.06	
Nesquehonite	22.52	24.25		23.39	24.22		23.10	24.25	
Dolomite	24.57	6.14		25.00	6.25	96	24.05	6.013	94
Diopside	12.87	15.95		13.17	15.87		13.20	15.75	

from the DFT–LDA results overall gives better results when compared to experiments.[56] Surprisingly, the elastic constants in the *ab* plane, C_{12}, and C_{13}, are very accurately calculated compared to DFT–LDA and experiments. However, C_{11} + C_{12} differs a lot from the experimental value of 334 GPa.[56] Also, C_{33} is calculated to be 165 GPa compared to the experimental value of 156 GPa. We note that our reactive interfacial FF gives reasonable results for the mechanical properties of magnesite when compared to the non-reactive thermodynamically consistent FF[25] that cannot properly capture the bulk modulus. It can be attributed to the choice of the magnesium charge that is taken less than +2.

The structure and mechanical properties of dolomite which were not part of the training set are calculated, and the results are shown in Table 5. Calcium parameters are taken from a previously fitted reactive FF for aqueous calcium carbonate systems with a fixed calcium charge of 2.[26] Compared to experimental values, the lattice parameters are overestimated by about 4% and 2%, respectively, for the interfacial and aqueous forcefields.[57] Based on the interfacial forcefield, the calculated bulk modulus is 96 GPa based on Voigt definition, slightly overestimating the experimental value of 94 GPa.[58] The aqueous FF gives poor results when it comes to the mechanical properties of dolomite. Based on our interfacial FF, the C_{11} constant is 183 GPa compared to 204 GPa based on Brillouin zone spectroscopy measurements.[59] Also, the calculated C_{33} constant is 96 GPa agrees well with the experimental value of 97 GPa. However, the rest of the elastic constants that are calculated by our forcefields are less accurate.

The rest of the solid phases in Table 5 are reasonably reproduced with both aqueous and interfacial forcefields in terms of lattice constants. Interestingly, brucite lattice constants are better captured with the aqueous FF. Especially in the c direction where the structure is layered, the lattice constant is only 1% deviating from the experiment, compared to the 10% underestimation of the interfacial FF. This discrepancy can be explained by the lower Mg–Ow bond lengths in the magnesium–water clusters used in the parameterization of the aqueous FF.

3.3 Surface hydration

The interaction of water with metal-containing rocks is crucial to understand CO_2 sequestration,[60] electrochemical reactions,[61] and accretion of the Earth from the water adsorption on dust grains,[62,63] *etc.* However, our knowledge of the mineral–water interface is limited due to experimental and theoretical difficulties. Here, we select three crystals, namely forsterite, magnesite, and magnesium oxide, to examine the fitted FF to predict the geometric structure of dry and hydrated surfaces. We use (010) cleaved surface of forsterite which was previously shown to have the lowest surface energy.[64] For magnesite, we choose the (10$\bar{1}$4) surface cleavage that is shown by scanning electron microscopy analyses to be the dominant surface.[65] For MgO, we choose the (001) surface. Only the top two layers of magnesium in all crystals are allowed to move while fixing the bottom layers to represent the bulk-like crystals.

The dry surfaces are relaxed using DFT and the interfacial reactive forcefield, as shown in Fig. 2a–f. On the forsterite surface, the top magnesium layer displaces toward the bulk phase for about 0.26 Å and 0.29 Å using DFT and ReaxFF, respectively. This results from the fact that the surface magnesium is undercoordinated and is attracted toward the negatively

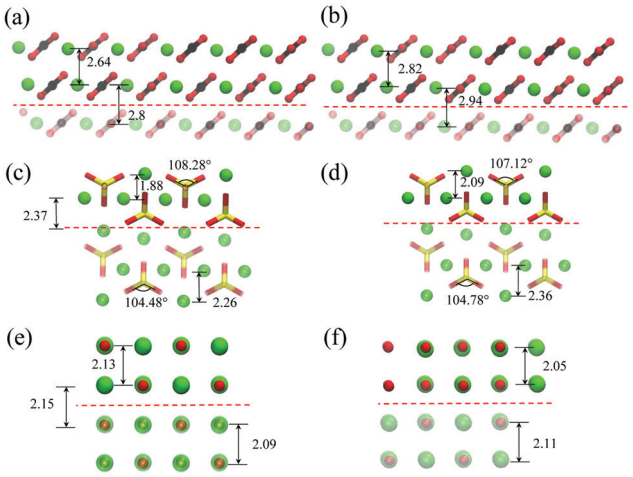

Fig. 2 The dry surface of magnesite, forsterite, and magnesia. (a) The dry (10$\bar{1}$4) surface of magnesite calculated from PBE-D3. The distance between magnesium layers in the bulk phase is 2.77 Å. (b) The dry (10$\bar{1}$4) surface of magnesite as calculated with ReaxFF. The distance between magnesium layers in the bulk phase is 2.80 Å. (c) The dry (010) surface of forsterite calculated from PBE-D3. (d) The dry (010) surface of forsterite calculated from ReaxFF. (e) The dry (100) surface of magnesia (MgO) calculated from PBE-D3. (f) The dry (100) surface of magnesia (MgO) calculated from ReaxFF. The black and red values refer to PBE-D3 and ReaxFF calculations, respectively. The atoms below red dashed lines are fixed, while the top atoms are able to move. Magnesium, carbon, oxygen and silicon colored as green, black, red and yellow, respectively. Distances are in Angstroms.

charged oxygens in the bottom layer. Also, the second top magnesium layer displaces slightly toward the surface for about 0.11 Å and 0.02 Å using DFT and ReaxFF, respectively. ClayFF, a classical FF with fixed charges, shows a displacement of 0.34 Å toward the bulk phase and 0.05 Å toward the surface for the first and second magnesium layers. The top silicon atoms move upward for about 0.19 Å, and the oxygen–silicon–oxygen angle changes from 104.48° to 108.28°. Using ReaxFF, the top silicon atoms move outward for about 0.07 Å, and the angle changes from 104.78° to 107.12°. This results from the lower equilibrium bond distance between undercoordinated magnesium and silicate oxygens. Also, the angle change can significantly reduce the stability of surface silicate groups and can potentially give rise to the production of carbonate groups when CO_2 is in the surface vicinity. DFT results are in close agreement with a previously reported DFT work[66] that used D2 dispersion correction.

The surface features of carbonate minerals like calcite, magnesite, and dolomite are important for modeling the dissolution/precipitation processes in the geological carbon cycle. Magnesite and dolomite surface reactivity has been investigated experimentally using surface complexation models.[65,67] However, reactive molecular simulations are yet applied to study these problems. According to our calculations on the magnesite's dry surface, slight displacement is found on the $(10\bar{1}4)$ surface, compared to Calcite ($CaCO_3$) which has a lower bulk modulus of about 73.5 GPa.[68] Upon DFT calculations, the first magnesium layer moves toward the bulk phase by about 0.11 Å, and the second magnesium layer moves away from it by 0.03 Å. With ReaxFF, the first magnesium layer moves toward the inner layers by about 0.1 Å, and the second magnesium layer moves away from the bulk phase by 0.02 Å, in full agreement with the DFT calculations. The CO_3 also distorts slightly, akin to the observations in the DFT simulations.

We also test our FF to reproduce the MgO(001) surface. MgO has critical industrial applications such as heterogeneous catalysis and concrete construction.[69–71] Based on our calculation, the anhydrous (001) surface of MgO changes only slightly. Based on our DFT calculations, we observe that the first magnesium layer displaces 0.16 Å out of the surface, while the second layer displaces only for 0.06 Å. Our ReaxFF simulations underestimate the displacement of the first and second magnesium layers by 0.09 Å and 0.05 Å, respectively.

After relaxing the dry surfaces, we add a water molecule on top of crystal surfaces and relax them using PBE-D3 and ReaxFF. Two configurations of water are found on each crystal surface, as shown in Fig. 3a–f without dissociating. On the forsterite(010) surface, a water molecule can either donate a hydrogen bond to a onefold coordinated silicate oxygen or donate two bonds to two onefold coordinated silicate oxygen as shown, respectively in Fig. 3a and b. We call the former case "side water" and the latter case "flat water". In both cases, the water oxygen is found coordinated around a surface magnesium. The adsorption energy based on PBE-D3 calculations for the "side water" and the "flat water" are respectively −0.90 eV and −1.34 eV. The calculated adsorption energies are less exothermic than those calculated through DFT with D2 dispersion correction, which produced −1.48 eV and −1.42 eV for "flat water" and "side water" configurations, respectively.[66]

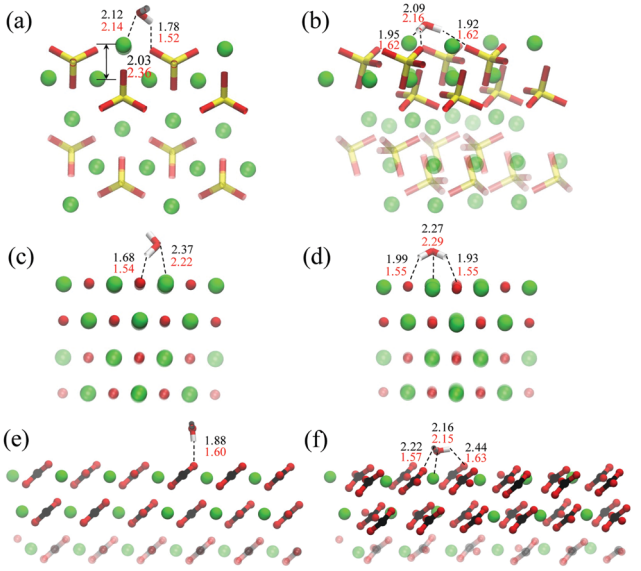

Fig. 3 The hydrated surface of magnesite, forsterite, and magnesia. The adsorption of water on the (010) surface of forsterite with (a) side and (b) flat configurations. The adsorption of water on the (100) surface of magnesia with (c) side and (d) flat configurations. The adsorption of water on the $(10\bar{1}4)$ surface of magnesite with (e) side and (f) flat configurations. The transparent atoms are held fixed during the simulation, while the rest of the atoms are free to move. Magnesium, carbon, oxygen and silicon colored as green, black, red and yellow, respectively. The distance values in black and red are derived from PBE-D3 and ReaxFF. Distances are in Angstroms.

The adsorption energies for the "flat water" and "side water" configurations based on ReaxFF are −2.38 eV and −1.6 eV, respectively. The aqueous FF gives even worse predictions about twice the amount for the interfacial FF, although the former gives accurate hydration energies of solvated magnesium in water. Although assigning a charge less than +2 to the less ionic magnesium in the crystal partially resolves this problem, we believe that the observed difference in water adsorption energies between PBE-D3 and ReaxFF roots in the hydration of silicate groups. The lower ReaxFF hydroxylation energy of water on silicates compared to DFT calculations[72] support the evidence. This discrepancy can be alleviated by further improving ReaxFF's Si/O/H parameter set to include water geometry and adsorption energy on silicates.

For the case of "side water," surface magnesium is displaced away from the surface by 0.45 Å and 0.27 Å calculated from PBE-D3 and ReaxFF, respectively, most probably due to the charge transfer caused by the water molecule. Using interfacial ReaxFF, the length of the donated hydrogen bond for the "flat water" is underestimated by about 0.3 Å compared to our PBE-D3 results. Also, the bond between surface magnesium and the water oxygen is overestimated by about 0.02 Å and 0.07 Å for the "side water" and "flat water," respectively, using the interfacial reactive FF compared to the PBE-D3 simulations. This difference is due to the overestimated magnesium–water

bond distance in our parameterization. The donated hydrogen bond in the "side water" configuration is 0.2 Å shorter in ReaxFF compared to PBE-D3. However, the magnesium water distance, in this case, is only 0.02 Å overestimated with ReaxFF compared to DFT.

Similar to the forsterite surface, the hydrogen bonds on the MgO surface are shorter when modeled with ReaxFF compared to PBE-D3, as shown in Fig. 3c and d. The hydrogen bond formed between the water hydrogen and the undercoordinated oxygen on the surface is 1.54 Å resulted from ReaxFF, compared to the 1.68 Å calculated *via* PBE-D3. Contrary to forsterite cases, the magnesium–water distance on MgO surface is underestimated by ~0.15 Å. Also, the hydrogen bonds of the "flat water" case are shorter by almost ~0.45 Å in ReaxFF compared to PBE-D3 values, although the magnesium oxygen bond is properly calculated. This shows that the water dipole moment is more oriented toward the surface in ReaxFF. According to our energy calculations at 0 K, the structure of "side water" is more stable than "flat water" opposite to the forsterite adsorption cases. The adsorption energies derived using PBE-D3 are −0.42 eV and −0.48 eV for "flat water" and "side water", respectively. Similar to the forsterite surface, the adsorption energies from interfacial ReaxFF are more exothermic than adsorption energies resulted from PBE-D3 by −1.38 eV and −1.70 eV.

On the surface of magnesite, the adsorption energies for the "flat water" and "side water" with PBE-D3 are −0.64 eV and −0.19 eV, respectively. However, ReaxFF-derived adsorption energies for "flat water" and "side water" are −1.55 eV and −0.48 eV overestimating their magnitude compared to their corresponding values from PBE-D3 calculations. The magnesium distance to the water oxygen simulated from ReaxFF is close to its value from PBE-D3, although the hydrogen bond distances are smaller in ReaxFF than PBE-D3.

Moving away from the single water adsorption, we examine the cases where 1 to 5 monolayers of water exist on the (010) surface of forsterite. In the corresponding ReaxFF simulations, all the one-folded silicate oxygen atoms become hydrated. Moreover, previous DFT simulations of the[73] surface of MgO have shown that a complete monolayer of water hydroxylates the surface.[74] We calculate the adsorption energy for various monolayers on the surface of forsterite, as demonstrated in Fig. 4. Since the adsorption energy of the first monolayer was substantially high due to interactions with the silicates, we only present the difference in the adsorption energy of n water monolayers (n = 2,3,4,5) and the adsorption energy of one monolayer. Comparison with experiment and modified ClayFF potential,[24] a non-reactive forcefield, shows that two and three monolayers of water give the best adsorption energies when subtracted from the adsorption energy of a single monolayer, and it is in an acceptable experimental range when four and five monolayers are present on the surface.

3.4 Ion pairing

The formation of $MgCO_3$ and $[MgHCO_3]^+$ ion pairs in the solution is a precursor for the nucleation of magnesium carbonate.[75,76] However, the molecular mechanism that leads to the nucleation and growth of crystalline or amorphous magnesium carbonate phases at different thermodynamic conditions and thin water films is not known.[8,9,17,76,77] Also, the attachment of carbonate to the surface magnesium on crystals like forsterite can lead to dissolution, known as ligand-promoted mineral dissolution.[78] Therefore, studying the energetics of the pairing reactions becomes crucial to understand homogeneous and heterogeneous nucleation and growth.[13]

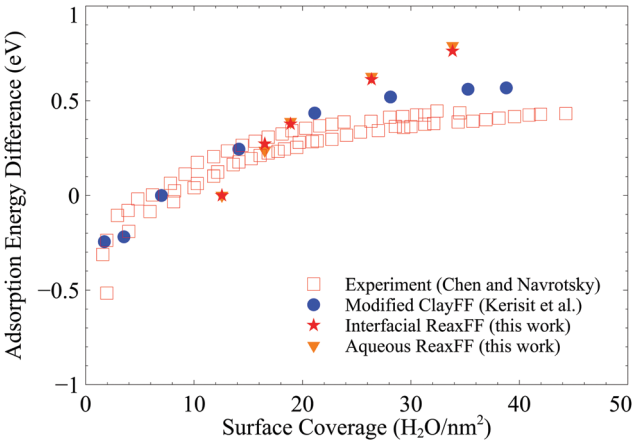

Fig. 4 The monolayer water adsorption energy difference on the surface of forsterite from simulations and experiments. The energy difference refers to the adsorption energy of n monolayers of water subtracted by the adsorption energy of one monolayer water (n = 2,3,4,5).

Here, we examine the fitted aqueous FF to model the structure of the separated ions (SI), solvent separated ion pairs (SSIP), and contact ion pairs (CIP) and their relative potential energy. We use recent geometries[12] calculated by DFT for hydrated Mg^{2+} and HCO_3^-/CO_3^{2-} in SI, SSIP, and CIP form as initial structures and relax them using energy minimization with our aqueous reactive FF. The resulting structures are shown in Fig. 5a–d. The relative energies between SSIP and CIP structures from our reactive simulations are compared to MP2/aD level and B3LYP/aD level calculations[12] in Table 6. As shown, the relative energies derived from our FF are within the acceptable range of the DFT results. However, SSIP structures are more stable than CIP contrary to the DFT results and infrared spectroscopic measurements in the solution.[79] Nevertheless, nucleation either takes place in the solution or at the mineral–water interface. Therefore, it is essential to test the FF in the solution and measure the relative stability of SSIP and CIP structures.

To this end, we construct a cubic box containing 560 water molecules and run MD at 298.15 K. First, we relax the cell in constant isobaric isothermal ensemble (*NPT*) using the Nose–Hoover thermostat and barostat with 0.5 fs timestep and relaxation time of 10 fs. Upon convergence in the box dimensions, we relax the system in canonical ensemble (*NVT*) at 298.15 K. Then, we place one magnesium ion and one carbonate ion at some distance in the solution and run MD for 6 ns. We observe that the relative distance between the two ions changes during the course of the simulation, and at random periods the two ions form an SSIP structure. In this simulation, we do not observe the

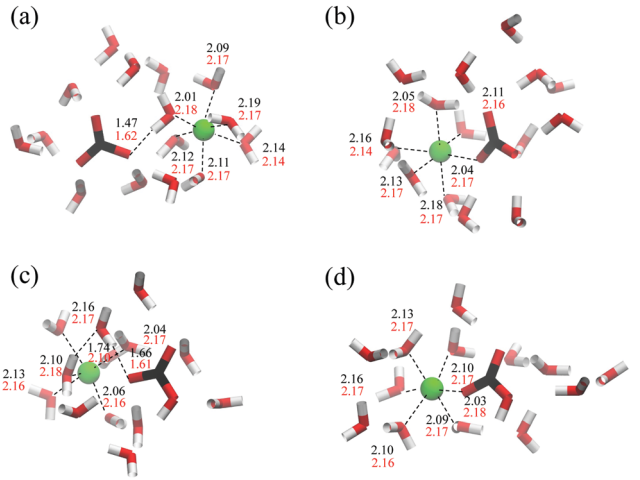

Fig. 5 Magnesium–(bi)carbonate ion pairing clusters. (a) Mg–CO_3 solvent separated ion pair. (b) Mg–CO_3 contact ion pair. (c) [Mg–HCO_3]$^+$ solvent separated ion pair (d) [Mg–HCO_3]$^+$ contact ion pair. The distance values in black and red are derived from PBE-D3 and ReaxFF, respectively. Distances are in Angstroms.

Table 6 Reaction energies for the conversion of seperated ions (SI) to contact ion pair (CIP) and solvent separated ion pair (SSIP) calculated from ReaxFF compared to DFT results with B3LYP/aD and MP2/aD functionals

	MP2/aD[a] (kcal mol^{-1})	B3LYP/aD[a] (kcal mol^{-1})	ReaxFF (kcal mol^{-1})
SI to CIP (CO_3)	−348.6402	−339.2884	−235.9648
SI to CIP (HCO_3)	−216.0981	−212.1398	−141.6936
SI to SSIP (CO_3)	−331.5982	−325.8616	−236.1492
SI to SSIP (HCO_3)	−200.5453	−192.3124	−148.0037

[a] Results from ref. 10.

formation of CIP structure as it is not expected to occur at room temperature due to the very rigid hydrated structure of magnesium and the limited MD timescales. Alternatively, we initialize the MD simulation with CIP structure and run for 6 ns. The CIP structure remained stable during the simulation. Also, the magnesium atom in the CIP structure has five water molecules, one water molecule less than the SSIP structure in agreement with experiments and FF calculations.[25,80] The potential energy of the CIP structure was on average 0.09 eV lower than the SSIP structure, and 0.13 eV lower than the case where ions were at least 3 water molecules apart from each other, confirming the relative stability of the CIP structure compared to SSIP and SI in the solution. Our results are consistent with the experiment that shows magnesium carbonate ion pair dissociates with 0.09 eV enthalpy difference.[81]

4. Applications of aqueous and interfacial FFs

4.1 H_2CO_3 dissociation in water with $Mg(OH)_2$

Atmospheric carbon dioxide naturally dissolves in water and partially reacts with it to produce carbonic acid and bicarbonate. The excess amount of CO_2 from burning fossil fuels can negatively impact natural processes, one of which is the acidification of the surface ocean. Carbonic acid dissociates to bicarbonate and proton, which reacts with carbonates on the oceanic surfaces that can severely slow down the growth of coral reefs.[82] However, alkaline earth metals can neutralize carbonic acid by forming carbonate minerals.[83]

Here, we investigate the carbonic acid dissociation to bicarbonate and carbonate in the presence of dissolved magnesium hydroxide $Mg(OH)_2$ in the water using our reactive FF. To this end, we relax a neutral cell consisting of 250 water molecules, a carbonic acid molecule, and an $Mg(OH)_2$ ion pair in *NPT* ensemble at room temperature and zero pressure using Nose–Hoover thermostat and barostat with timestep of 0.25 fs. After relaxation in *NPT* ensemble, we run the system in *NVT* ensemble. We first observe that the hydroxide initially coordinated around magnesium readily diffuses out into the solution through Grotthuss mechanism. Nevertheless, carbonic acid remained intact in about 2 ns. Adding another $Mg(OH)_2$ monomer, resulted in a fast reaction between carbonic acid with one of the hydroxide ions in less than 1 ps to make bicarbonate as expected in such a basic solution, as shown in Fig. 6a–c. After about 100 ps, the other hydroxide structurally diffuses toward the bicarbonate and grabs its proton and produces a carbonate ion, as shown in Fig. 6a, d and e. Obviously because the hydroxide concentration is ~13 order of magnitude greater than its concentration at pH of 14, we cannot expect the carbonic acid dissociation to occur this rapidly. However, our simulations show that the hydroxide, which diffuses structurally at a high rate in bulk water can reach to carbonic acid to make a spontaneous proton transfer reaction. With our reactive FF, we also observed the diffusion of surface hydroxide on metal divalent containing minerals toward the carbonic acid at the thin water film. The limited space in the nano-meter thin film in this system can substantially increase the rate of carbonic-acid-to-carbonate reaction, although the diffusion of hydroxide in the structured water is hindered. This is the subject of next section where we take brucite as a model surface to study this reaction.

We calculate the RDF for the three stages of the simulation described above. First, we fix the Ox–H bonds of the carbonic acid and proceed with the simulation and output the trajectories. Then, we unfix one of the Ox–H bonds and let the proton transfer happen to turn carbonic acid to bicarbonate, and run the simulation again to produce outputs of the trajectories. Finally, we unfix the remaining Ox–H bond of the bicarbonate until it turns into carbonate through another proton transfer reaction. Again, we run the simulation and output the trajectories. For all the stages, we run the simulations in *NVT* ensemble at room temperature using Nose–Hoover thermostat with timestep of 0.25 fs and relaxation time of 25 fs. We output the trajectories every 25 fs over the course of 500 ps to produce enough data for the radial distribution function (RDF) calculations. We also calculate the RDF for Mg–Ow for the two solvated magnesium cations. The resulting RDFs are shown in Fig. 7a–d.

The RDF for Mg–Ow has one sharp peak at around 2.15 Å that corresponds to the first shell of water molecules that are tightly bound to the doubly charged magnesium cation as

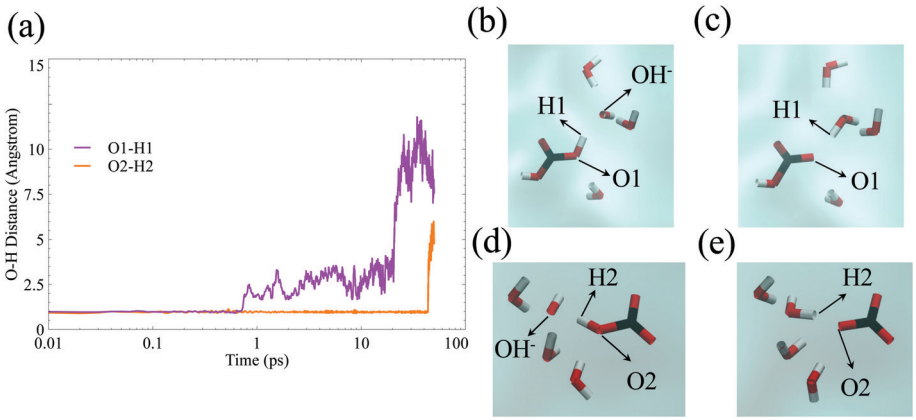

Fig. 6 Carbonic acid dissociation in the presence of magnesium hydroxide. (a) Time-reaction for the deprotonation of carbonic acid. O1, H1, O2, and H2 are shown in the snapshots on the right. (b) Carbonic acid in the solution before the reaction with the adjacent OH^- occurs (c) bicarbonate is formed as the product of the deprotonation of carbonic acid through reaction with solvated hydroxide ion. (d) Bicarbonate in the solution before the reaction with the adjacent OH^- occurs (e) carbonate is formed through the deprotonation of bicarbonate through reaction with a hydroxide. The cyan color in the background of snapshots represent the liquid water.

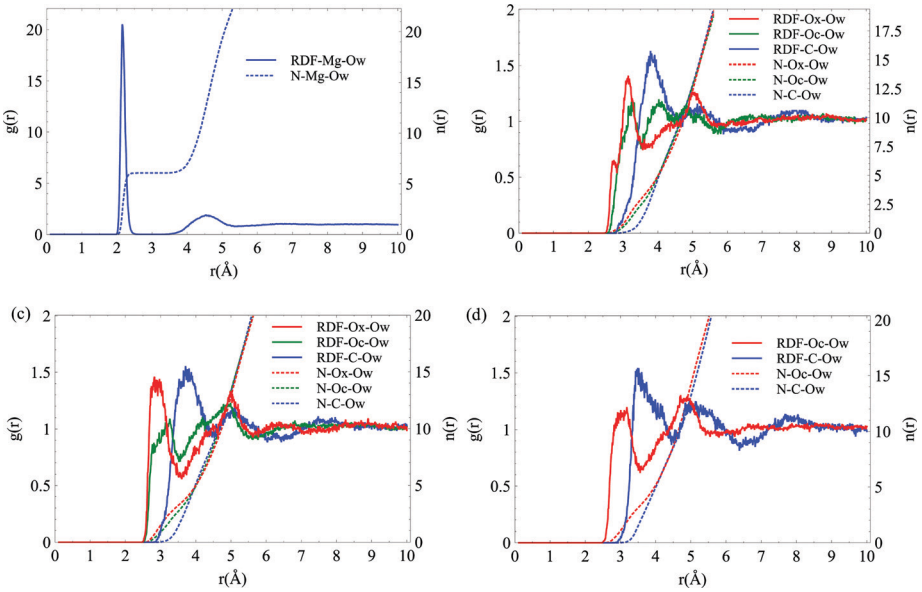

Fig. 7 $g(r)$ and coordination number, $n(r)$, for (a) magnesium (b) carbonic acid (c) bicarbonate and (d) carbonate in the solution. $g(r)$ is shown with solid line and $n(r)$ is shown with dashed lines in all figures. Ow, Ox and Oc refer to water oxygen, hydroxyl oxygen, and carbonyl oxygen, respectively.

shown in Fig. 7a. The water coordination number for magnesium is derived to be 6, which is in agreement with experiment[84] and previous simulations.[25,85] The carbonic acid contains two hydroxyl oxygen (Ox) and one carbonyl oxygen (Oc) which have different hydrogen bond networks as can be seen in the RDFs presented in Fig. 7b. The first large peak for Ox–Ow is located at 3.13 Å which corresponds to the hydrogen bond that are accepted by the carbonic acid hydroxyl groups. A smaller peak for Ox–Ow is observed at 2.75 Å that is related to the hydrogen bonds donated by the hydroxyl of the carbonic acid. The first peak for Oc–Ow is located at 3.25 Å. By integrating the RDFs up to 3.75 Å for the first shell of water molecules around Ox, a hydration number of 3.8 is derived, see $n(r)$ in Fig. 7b. The hydration number of Oc is 3.4, which is slightly smaller than that of Ox, due to the stronger hydrogen bonds around hydroxyl groups that both donate and accept hydrogen bonds. Probing the hydration structure of carbonic acid through experiment is difficult, because of its short lifetime. However, quantum mechanics/molecular dynamics (QM/MM) simulations of aqueous carbonic acid shows a hydration number of 3.17 for Oc, which is close to our calculated value of 3.4.[86]

For the bicarbonate simulation, the RDF for Oc and Ox are shown in Fig. 7c. The first peak for Ox–Ow is almost at 2.9 Å, while the first peak for Oc–Ow is slightly larger at around 3.1 Å, due to the stronger hydrogen bond of the hydroxyl oxygen. By integrating the RDF for the first peak up to 3.75 Å, the hydration number of Oc and Ox are derived to be 3.65 and 3.9, see the $n(r)$ values in Fig. 7c. These hydration numbers are both

higher than their counterparts in carbonic acid. This is due to the charge of bicarbonate compared to the neutral carbonic acid as suggested by X-ray absorption spectroscopy measurements and Car–Parrinello MD simulations.[86,87] However, our calculated hydration number for Oc is smaller than the derived value through QM/MM calculation which was 4.26.[86] This could in part results from the charge equalization method in ReaxFF that gives a lower charge magnitude of bicarbonate in our simulations, which is around −0.85 that its formal charge of −1.

We also calculate the RDF and hydration numbers for carbonate as shown in Fig. 7d. The first peak for the Oc–Ow is located at around 3.0 Å. Forcefield calculations done by Bruneval *et al.*[88] shows the peaks to be in a lower range at 2.69. The hydration number for Oc of the carbonate is 4.08 if we integrate the RDF up to 3.75 Å. The forcefield calculation by Bruneval *et al.* shows a hydration number of 4.3, which like for the bicarbonate case could result from the lower charge magnitude of bicarbonate in our simulation (~ -0.9) that its formal charge of −2.

4.2 Bicarbonate–brucite interaction

Ex situ carbon mineralization can be achieved through the carbonation of mine wastes such as brucite [$Mg(OH)_2$] in mafic and ultramafic mines.[4,89] One study estimated that the accelerated carbonation of brucite in mine tailing could offset 22–57% of mine emissions.[90] Here, we examine the interaction of bicarbonate at the water–brucite interface.

We construct a simulation cell containing a brucite slab and a slit pore filled with liquid water. We fix the inner layers of the brucite so that they represent the bulk structure, and we let the first two layers move and interact with the water molecules on top. The size of the box is 18.5 Å × 32.15 Å × 57.10 Å in *x*, *y* and *z* direction, respectively. Then, we place a bicarbonate ion at the water–brucite interface and perform MD simulations in the *NVT* ensemble while fixing O–H bonds in water and bicarbonate to relax the system. Then, we remove the constraint on the bonds and let the system evolve naturally. Similarly, on the hydroxylated (010) forsterite surface simulated through reactive molecular dynamics, we observe spontaneous diffusion of surface OH-groups in the water layers adsorbed to the surface, which is the subject of our future work.

Such proton transfer reactions were also observed on other oxide surfaces in both simulations and experiments. Through *ab initio* MD simulations,[91] it was shown that the rate of proton transfer reactions at the water–ZnO $(10\bar{1}0)$ surface substantially increases when the number of water layers increases from one layer to a liquid multi-layer. Also, *ab initio*-based deep neural network analysis was able to show long-range proton transfer through water molecules at the water–TiO_2 interface.[92] Moreover, scanning tunneling microscopy experiments on FeO[93] and TiO_2[94] monolayers and single-molecule localization microscopy on defective boron nitride layers[95] unveil the proton transport at the solid–water interface. Recently, spectral single-molecule scanning tunneling microscopy and *ab initio* simulations[96] demonstrated higher proton diffusivity along the surface of boron nitride when it is in contact with a binary water–methanol solution rather than water-only solution.

After few picoseconds in our simulation on the brucite surface, we observe that a hydrogen-bond network forms between the bicarbonate and a surface hydroxide leading to a chain of proton transfer reactions that deprotonates the bicarbonate at the end, as shown in Fig. 8a–d. The hydroxide ion structurally diffuses from the surface toward the bicarbonate in the interfacial water film. Structural diffusion, often called ''Grotthuss diffusion,'' is the hopping of a proton from a hydronium ion to a neighboring water molecule or from a water molecule to a neighboring hydroxide. It involves breakage and formation of O–H bonds as the proton migrates between water molecules. It is much faster than vehicular diffusion. The centers of charge and mass move together.[97] Similarly, hydroxide groups can structurally diffuse through water molecules as observed in biological systems and enzymatic reactions.[98,99]

We also calculate the RDF for surface magnesium, carbonic acid, bicarbonate, and carbonate for the simulation on the surface of brucite. Initially, we fix the carbonic acid in the water layers 5 Å away from the surface of brucite. To avoid spontaneous proton transfer that transforms the carbonic acid to bicarbonate and then to carbonate, we fix the O–H bonds of the hydroxyl group in carbonic acid. We run the simulation in *NVT* ensemble for 250 ps, and output the trajectories every 25 fs to produce data for RDF calculation. Other simulation settings are similar to those we used for carbonic acid deprotonation described in Section 4.1.

The RDF for surface magnesium (Ms) and oxygen of water and surface hydroxide (O*) is shown in Fig. 8e. The first peak is located at 2.13 Å, and a coordination number of 2.7 is derived for the first shell of O*, where two surface hydroxides are always present. The RDFs calculated for carbonic acid on the surface are shown in Fig. 8f. Like carbonic acid in the solution, the RDF for Ox–O* has two peaks close to each other, one at 2.6 Å that corresponds to the accepted hydrogen bond and another at 3.12 that corresponds to the donated hydrogen bond. Interestingly, the hydration number for Ox is about 5.3 which is significantly larger than its counterpart in the solution which is 3.8. This can be the result of denser water layers with stronger hydrogen bonds compared to liquid water. This could also be the reason for the RDF for Oc–O* to have its first two peaks closer to each other than what we observe in the solution.

For the case of bicarbonate in the water layers on top of brucite, we see that the first peaks for both RDFs of Ox–O* and Oc–O* shift toward smaller distances as shown in Fig. 8g. We think this systematic shift is the result of different water permittivity in the water layers than that of liquid water. Therefore, compared to liquid water, the negative charge of bicarbonate results in stronger electrostatics field that strengthens hydrogen bonds with dipolar water molecules. As shown in in Fig. 8h, we could not observe any further shift for the doubly-charged carbonate, that is related to the smaller charge magnitude of carbonate ($\sim$1.05) than its formal charge of 2.

The ReaxFF simulations also provide a detailed picture of the dynamics of structural hydroxide diffusion on the brucite

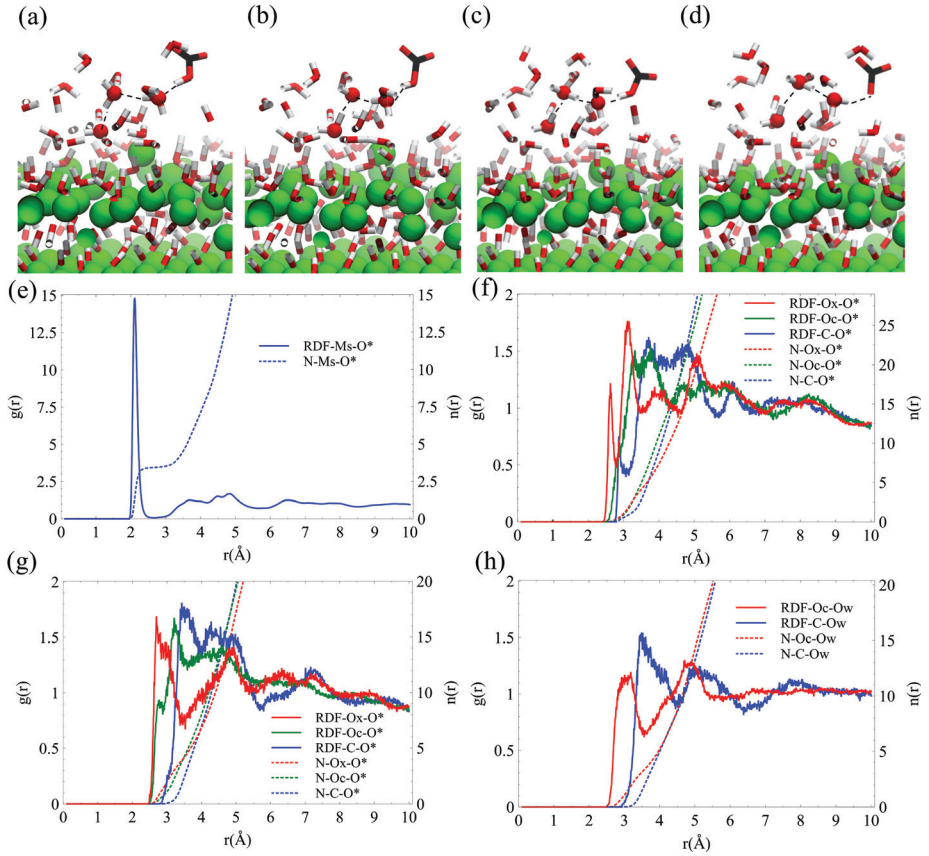

Fig. 8 The deprotonation of bicarbonate at the brucite–water interface. From (a) to (c) the hydroxide in the first water layer diffuses toward the bicarbonate. (d) The bicarbonate deprotonates to carbonate hydrating a neighboring hydroxyl group. (e) $g(r)$ and coordination number, $n(r)$, for magnesium–water on the surface of brucite. (f) $g(r)$ and $n(r)$ for carbonic acid on the surface of brucite. (g) $g(r)$ and $n(r)$ for bicarbonate on the surface of brucite. (h) $g(r)$ and $n(r)$ for carbonate on the surface of brucite. $g(r)$ is shown with solid line and $n(r)$ is shown with dashed lines in all figures. O*, Ox and Oc refer to water/surface hydroxide oxygen, hydroxyl oxygen, and carbonyl oxygen respectively. Ms represents surface magnesium.

surface. Since the adsorbed water layers on the brucite surface are more structured than liquid water, and also because the positively-charged magnesium cations attract hydroxide ions, we expect a hindered interfacial diffusion for hydroxide ions. To show this quantitatively, we run further simulations to calculate the diffusion constant of hydroxide ions adsorbed on the surface of brucite. To this end, we calculate the diffusion constant of OH^- in XY direction, parallel to the brucite surface, and in the Z direction s perpendicular to the surface using the Einstein relation:

$$D_{xy} = \frac{1}{4t}\left\langle \left| r_{xy}(t) - r_{xy} \right|^2 \right\rangle \quad (11)$$

$$D_z = \frac{1}{t}\left\langle \left| r_z(t) - r_z \right|^2 \right\rangle \quad (12)$$

In which r represents the position of the particle, and t is the time. $\langle |r_{xy}(t) - r_{xy}|^2 \rangle$ and $\langle |r_z(t) - r_z|^2 \rangle$ are the mean-square displacement (MSD) in the XY plane and in the Z direction, respectively.

To calculate the MSD for hydroxide ions on the surface, we randomly pick seven hydroxides and track the trajectory of the O* of the OH^-.[73] The index O* can change during the course of the simulation as proton transfer can happen between water molecules and the OH^-. We construct a similar system as in Section 4.2, containing brucite slab in contact with water while letting the first two layers of brucite move and fix the inner layers. We initially relax the system in the *NVT* ensemble at room temperature for 200 ps using timesteps of 0.25 fs and a Nose–Hoover thermostat with relaxation time of 25 fs. After the system is relaxed, we change the ensemble to *NVE* to avoid thermostat effects that can interfere with the trajectory of atoms. We run the system for 125 ps, and output trajectories every 2.5 fs to be used for the calculation of MSD. The resulting MSD up to 30 ps for the seven randomly picked hydroxide ions are shown in Fig. 9a and b.

We note that the slope of the MSDs are not quite linear compared to the MSDs of hydroxide ions in liquid water resulted from the same forcefield.[73] This is due to the presence of magnesium cations on the surface of brucite that can trap the hydroxide ions. Here, we use the linear part of the MSDs with maximum slope for the calculation of diffusion constants. We calculate the diffusion constant for each O* from the linear parts of the resulted MSDs. For the diffusion in XY plane, D_{xy} ranges between 0.04 and 0.18 $Å^2\ ps^{-1}$, while D_z ranges between 0.16 and 0.76 $Å^2\ ps^{-1}$. Based on the similar ReaxFF forcefield

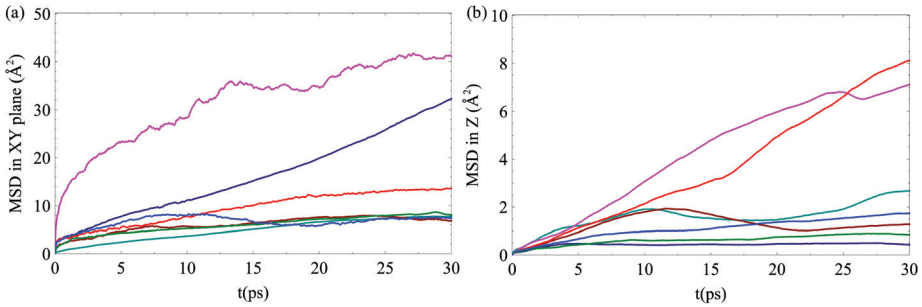

Fig. 9 Mean-square displacement (MSD) for hydroxide ions on the surface of brucite. (a) MSD in the *XY* plane parallel to the surface. (b) MSD in the *Z* direction perpendicular to the surface. Different colors represent the displacement of seven randomly picked hydroxide ions on the surface of brucite.

for water, the reported diffusion constant for the hydroxide ion in water is 1.03 $Å^2$ ps^{-1} which is higher than our calculated diffusion constants. This difference can arise from the more structured water layers on the hydrophilic surface of brucite. The difference between D_{xy} and D_z and the variable diffusion constant derived for each of the randomly selected hydroxide ions show anisotropy and heterogeneity in the interfacial diffusion process of these species in the adsorbed water layers. It is noteworthy that a second-generation ReaxFF water model can better predict the diffusion of hydroxide and hydronium ions compared to the one we used in our paper.[73] However, because the first generation ReaxFF water model is fitted and tested for the proton transfer between water and carbonic acid, which is essential for modelling magnesium carbonate systems, we use the first generation ReaxFF water model. Nevertheless, we carefully analyzed the proton transfer between bicarbonate and forsterite surface using both first- and second-generation ReaxFF water model. We find that the free energy barrier for the long-range proton transfer that transforms bicarbonate to carbonate is not significantly affected by the water model.

4.3 Free energy calculation of Mg–CO_3 surface complex formation on the surface of forsterite

The knowledge of the thermodynamics of ion-pairing at the solid–liquid interface is critical for understanding heterogeneous nucleation and growth. However, ion-pairing in the solution and at the solid–liquid interface is experimentally challenging to probe due to the small size of the ions and their short lifetime. On the other hand, quantum mechanical calculations are also problematic due to their high computational cost and the uncertainty about van der Waals interactions in the liquid phase. Nonetheless, molecular simulations can provide insight into the kinetics of ion interactions if accurate FFs are available. A thermodynamically stable FF was successfully able to calculate the free energy barrier for the pairing of (Ca^{2+}, Mg^{2+}, Sr^{2+}) cations and bicarbonate and carbonate species in the solution. However, metal cations on the surface of metal-silicates and metal-oxides are sometimes coordinated with hydroxide ions. Therefore, surface complex formation with ions like carbonate and bicarbonate may require a proton transfer reaction from the first shell of metal cations to their second shell, especially for magnesium cations tightly bound to their water/hydroxide shell. This calls for a reactive FF like ReaxFF, which can model the structural diffusion of proton/hydroxide.

Here, we do the free energy calculation for the carbonate adsorption on the (010) hydroxylated surface of forsterite. First, we construct a slab of forsterite with 9 layers and an interlayer space with a size of 27 Å. We fill the interlayer space with water such that the density at the middle 10 Å is 0.91 g cm^{-3} consistent with the density of liquid water when relaxed with ReaxFF. We fix the forsterite slab except for the first two surface layers at the top and the bottom. The energetics of the adsorption of carbonate on the forsterite surface is determined *via* the umbrella sampling (US) technique as implemented in the "PLUMED 2.5" add-on package to LAMMPS.[100] Here, we use a biased harmonic spring with a stiffness of 140 kcal mol^{-1} $Å^{-2}$ between the center of mass of the carbonate and a fixed reference Me^{2+} atom in the inner layer of forsterite respectively. The normal distance to the solid surface is taken as the "collective variable" and sampling windows are separated by 0.1 Å. Histograms of the distribution of the collective variables were produced after 100 ps of equilibration phase, and another 250 ps of the production phase of MD runs at 300 K in the *NVT* ensemble. The substrate (except the first two layers) were fixed. A weak harmonic potential was also considered in the '*xy*' plane (parallel to the surface) to keep the carbonate in the desired adsorption site, enclosed in a cylinder. The free energy difference is then obtained *via* the weighted histogram analysis method (WHAM).[101]

Our PMF calculations show that the formation of Mg$\equiv$$CO_3$ surface complex on a random Mg site is relatively stable. This surface complex formation is made possible through a proton transfer step in which the OH^- attached to the surface grabs a proton from the second water shell. Another water molecule leaves the first shell to make room for the carbonate (see Fig. 10a–c). The energy barrier for this Mg–CO_3 surface complex formation is 0.21 eV, about 0.04 eV lower than the free energy required for their pairing in bulk water.[25] This has major implications on the nucleation stage. It reduces the magnesium dissolution energy barrier and can enhance the growth of magnesite crystal since ion pairs could readily attach to the crystal. This can also help explain the anomalous low activation energy barrier for the nucleation and growth of magnesite at

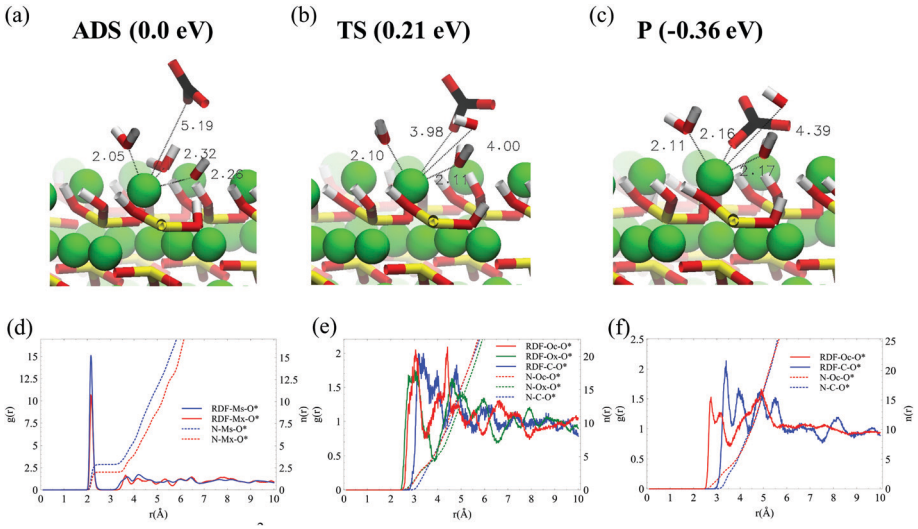

Fig. 10 Adsorption of CO_3^{2-} on hydroxylated{010} surface of Forsterite. (a–c) (ADS) adsorbate state of CO_3^{2-} as determined by PMF calculations. Two water molecules as well as one hydroxide are coordinated around surface magnesium. (TS) transition state. (P) product state. (d) $g(r)$ and coordination number, $n(r)$, for (d) magnesium (e) bicarbonate and (f) carbonate on the surface forsterite. $g(r)$ is shown with solid line and $n(r)$ is shown with dashed lines in all figures.

low temperature[17] when reactions occur at the thin water film formed on forsterite.

We calculate the RDF for surface magnesium and carbonate at two windows that we used for the free energy calculation: (1) when the carbonate is 5 Å away from the surface. (3) When the carbonate is adsorbed on the surface and is paired with two surface magnesium atoms. The first peak of RDF for the surface magnesium (Ms) and water is located at 2.15 Å similar to the location of the water in the first hydration shell of magnesium solvated in water as shown in Fig. 10d. The water coordination number for Ms is 2.85. We label the surface magnesium that is coordinated with carbonate as Mx as shown in Fig. 10d. Although, the location of the first peak for Mx–O* is the same as Ms–O*, the water coordination number for Mx is dropped to 2. As stated in the previous paragraph, we observe that for the magnesium–carbonate surface complex formation, the coordinated hydroxide grabs a proton from a nearby water molecule, and one water molecule is removed from the first coordination shell of Mx. When the carbonate is adsorbed on the surface, we need to differentiate two carbonate oxygens that are paired to surface magnesiums (Ox) with the one that is oriented toward the solution (Oc). As shown in Fig. 10e, the hydration number for Oc is $\sim$4.3, which is higher than the hydration number for oxygens of the carbonate in the solution, due to the higher density of layered water on top of forsterite. When the carbonate is distanced 5 Å from the surface, we observe two peaks in the RDF for Oc–O* as shown in Fig. 10f. By visual inspection, we find that the carbonate is not able to rotate freely as in the solution, due to the electrostatic field it senses from the surface magnesium. Rather, one carbonate oxygen remains oriented toward to the surface for the entire time of the simulation. The hydration number of the carbonate oxygen (Oc) is 4.3, higher than its solution counterpart.

3. Conclusion

We develop two reactive FFs for modeling aqueous magnesium carbonate and Mg/O/Si/C/H containing solids and their interfaces with water. We successfully parameterize the FFs to the configurations and mechanical properties of magnesite, magnesium hydroxide, magnesium oxide, and other relevant crystals. Additionally, the structures and hydration energies of magnesium are included in the list of observables for the aqueous FF. After deriving the FF parameters, we test the transferability of the interfacial FF to other prevalent magnesium-containing minerals in the context of carbon sequestration, including the bulk structure of forsterite, nesquehonite, dolomite, and diopside. Not only the lattice properties of these crystals are captured well with our FF, but also the bulk modulus of dolomite and some of its elastic constants are predicted accurately.

Next, the interfacial structure of magnesium (-carbonate, -silicate, and -oxide) minerals when dry or in contact with a single water molecule are investigated using both DFT calculations and interfacial ReaxFF. Although the geometry of all dry surfaces is similar in both methods, the hydration energies are overestimated when calculated through the reactive FF. Some hydrogen bonds are underestimated, except for the case of "side water" adsorption on the surface of forsterite. The discrepancy of hydration energies and hydrogen bond distances stems partly from the oxygen–hydrogen interaction parameters in ReaxFF that are mainly fitted to describe liquid water, and partly from the absence of Mg–O–O and Mg–O–H parameters in our forcefield. Unlike the single water molecule adsorption, the adsorption energies resulted from ReaxFF for two to five water monolayers are in agreement with the experiment. This makes our FF suitable to study reactions at the water–forsterite interface when few water monolayers are present.

Then, we study the interaction of magnesium and (bi)carbonate in gaseous clusters and liquid water. Our calculations for magnesium–(bi)carbonate ion-pairing through the fitted aqueous FF agree well with DFT results. Although the obtained energies for SSIP structures are lower than the CIP structure in gaseous clusters, the averaged potential energies in liquid water confirm the relative stability of CIP to SSIP and SSIP to SI structures. This enables our force field to study homogeneous nucleation of magnesite, hydromagnesite, nesquehonite, and amorphous magnesium carbonate phases. We also check the applicability of the derived reactive forcefields for the dissociation of carbonic acid in liquid water that contains magnesium and hydroxide ions and the interfacial water layers on top of the brucite surface. Our simulations demonstrate the migration of hydroxide ions that leads to carbonate production, whether in liquid water or at the interface of brucite. Proton transfer reactions at the interface of metal oxides have been previously observed through both experiments and quantum mechanical calculations.

The observed proton transfer at the hydroxylated-solid–water interface has significant implications on the nucleation of magnesium carbonate phases at geological conditions. It can explain the anomalously low activation energy barrier for the formation of magnesite. At the molecular scale, it can manifest both through the pairing of the dissolved surface magnesium and carbonate at the thin water film or the formation of neutral magnesium–carbonate surface complexes that can dissolve faster than the magnesium cation.[12] Here, we show that a stable $Mg–CO_3$ surface complex can form on the hydroxylated surface of forsterite with a low energy barrier. However, more elaborate free energy calculations that consist of magnesium–water coordination number as a collective variable are needed for more accurate energy barrier calculations.

Data availability

The modified LAMMPS source code for constant cation charge ReaxFF simulations are available upon request from the corresponding author.

Conflicts of interest

The authors declare no competing interests.

Acknowledgements

This work was primarily supported by Early Career Award Program from the DOE Office of Science, Basic Energy Sciences, Division of Chemical, Biological and Geological Sciences under contract no. DE-SC0022301. The brucite calculations are supported by the National Science Foundation under Awards No. CMMI-2103125. Any Opinions, findings and conclusions or recommendations expressed in this material are those of the authors and do not necessarily reflect those of the funding agencies. MJAQ also gratefully acknowledges financial support through Hellman Fellowship. We thank Drs. Andreas Funk and Quin Miller for fruitful discussions.

References

1 J. J. R. F. da Silva and R. J. P. Williams, *The Biological Chemistry of the Elements: The Inorganic Chemistry of Life*, OUP, Oxford, 2001, p. 606.
2 A. I. Taub and A. A. Luo, Advanced lightweight materials and manufacturing processes for automotive applications, *MRS Bull.*, 2015, **40**(12), 1045–1054.
3 D. Höche, S. V. Lamaka, B. Vaghefinazari, T. Braun, R. P. Petrauskas and M. Fichtner, *et al.*, Performance boost for primary magnesium cells using iron complexing agents as electrolyte additives, *Sci. Rep.*, 2018, **8**(1), 7578.
4 S. Ó. Snæbjörnsdóttir, B. Sigfússon, C. Marieni, D. Goldberg, S. R. Gislason and E. H. Oelkers, Carbon dioxide storage through mineral carbonation, *Nat. Rev. Earth Environ.*, 2020, **1**(2), 90–102.
5 M. Pavlov, P. E. M. Siegbahn and M. Sandström, Hydration of Beryllium, Magnesium, Calcium, and Zinc Ions Using Density Functional Theory, *J. Phys. Chem. A*, 1998, **102**(1), 219–228.
6 G. D. Markham, J. P. Glusker and C. W. Bock, The Arrangement of First- and Second-Sphere Water Molecules in Divalent Magnesium Complexes: Results from Molecular Orbital and Density Functional Theory and from Structural Crystallography, *J. Phys. Chem. B*, 2002, **106**(19), 5118–5134.
7 J. Xu, C. Yan, F. Zhang, H. Konishi, H. Xu and H. H. Teng, Testing the cation-hydration effect on the crystallization of Ca–Mg–CO3 systems, *Proc. Natl. Acad. Sci. U. S. A.*, 2013, **110**(44), 17750–17755.
8 O. Qafoku, D. A. Dixon, K. M. Rosso, H. T. Schaef, M. E. Bowden and B. W. Arey, *et al.*, Dynamics of Magnesite Formation at Low Temperature and High pCO2 in Aqueous Solution, *Environ. Sci. Technol.*, 2015, **49**(17), 10736–10744.
9 O. Qafoku, J. Hu, N. J. Hess, M. Y. Hu, E. S. Ilton and J. Feng, *et al.*, Formation of submicron magnesite during reaction of natural forsterite in H2O-saturated supercritical CO2, *Geochim. Cosmochim. Acta*, 2014, **134**, 197–209.
10 A. R. Felmy, O. Qafoku, B. W. Arey, J. Z. Hu, M. Hu and H. Todd Schaef, *et al.*, Reaction of water-saturated supercritical CO2 with forsterite: Evidence for magnesite formation at low temperatures, *Geochim. Cosmochim. Acta*, 2012, **91**, 271–282.
11 Q. R. S. Miller, E. S. Ilton, O. Qafoku, D. A. Dixon, M. Vasiliu and C. J. Thompson, *et al.*, Water Structure Controls Carbonic Acid Formation in Adsorbed Water Films, *J. Phys. Chem. Lett.*, 2018, **9**(17), 4988–4994.
12 Q. R. S. Miller, D. A. Dixon, S. D. Burton, E. D. Walter, D. W. Hoyt and A. S. McNeill, *et al.*, Surface-Catalyzed Oxygen Exchange during Mineral Carbonation in Nanoscale Water Films, *J. Phys. Chem. C*, 2019, **123**(20), 12871–12885.

13 J. S. Loring, J. Chen, P. Bénézeth, O. Qafoku, E. S. Ilton and N. M. Washton, *et al.*, Evidence for Carbonate Surface Complexation during Forsterite Carbonation in Wet Supercritical Carbon Dioxide, *Langmuir*, 2015, **31**(27), 7533–7543.
14 Q. R. S. Miller, H. T. Schaef, J. P. Kaszuba, G. Gadikota, B. P. McGrail and K. M. Rosso, Quantitative Review of Olivine Carbonation Kinetics: Reactivity Trends, Mechanistic Insights, and Research Frontiers, *Environ. Sci. Technol. Lett.*, 2019, **6**(8), 431–442.
15 E. Placencia-Gómez, S. N. Kerisit, H. S. Mehta, O. Qafoku, C. J. Thompson and T. R. Graham, *et al.*, Critical Water Coverage during Forsterite Carbonation in Thin Water Films: Activating Dissolution and Mass Transport, *Environ. Sci. Technol.*, 2020, **54**(11), 6888–6899.
16 Q. R. S. Miller, J. P. Kaszuba, S. N. Kerisit, H. Todd Schaef, M. E. Bowden and B. Peter McGrail, *et al.*, Emerging investigator series: ion diffusivities in nanoconfined interfacial water films contribute to mineral carbonation thresholds, *Environ. Sci.: Nano*, 2020, **7**(4), 1068–1081.
17 Q. R. S. Miller, J. P. Kaszuba, H. T. Schaef, M. E. Bowden, B. Peter McGrail and K. M. Rosso, Anomalously low activation energy of nanoconfined MgCO 3 precipitation, *Chem. Commun.*, 2019, **55**(48), 6835–6837.
18 T. Liu, S. Gautam, H.-W. Wang, L. M. Anovitz, E. Mamontov and L. F. Allard, *et al.*, Structure and dynamics of water on the forsterite surface, *Phys. Chem. Chem. Phys.*, 2018, **20**(44), 27822–27829.
19 J. Zachara, S. Brantley, J. Chorover, R. Ewing, S. Kerisit and C. Liu, *et al.*, Internal Domains of Natural Porous Media Revealed: Critical Locations for Transport, Storage, and Chemical Reaction, *Environ. Sci. Technol.*, 2016, **50**(6), 2811–2829.
20 Q. Gautier, P. Bénézeth and J. Schott, Magnesite growth inhibition by organic ligands: An experimental study at 100, 120 and 146 °C, *Geochim. Cosmochim. Acta*, 2016, **181**, 101–125.
21 Q. R. S. Miller, J. P. Kaszuba, H. T. Schaef, M. E. Bowden and B. P. McGrail, Impacts of Organic Ligands on Forsterite Reactivity in Supercritical CO2 Fluids, *Environ. Sci. Technol.*, 2015, **49**(7), 4724–4734.
22 C. P. Morrow, A. A. Olsen and J. D. Kubicki, Quantum mechanical modeling of hydrolysis and H2O-exchange in Mg-, Ca-, and Ni-silicate clusters: Implications for dissolution mechanisms of olivine minerals, *Am. Mineral.*, 2014, **99**(11–12), 2303–2312.
23 V. Prigiobbe, A. Suarez Negreira and J. Wilcox, Interaction between Olivine and Water Based on Density Functional Theory Calculations, *J. Phys. Chem. C*, 2013, **117**(41), 21203–21216.
24 S. Kerisit, J. H. Weare and A. R. Felmy, Structure and dynamics of forsterite–scCO2/H2O interfaces as a function of water content, *Geochim. Cosmochim. Acta*, 2012, **84**, 137–151.
25 P. Raiteri, R. Demichelis and J. D. Gale, Thermodynamically Consistent Force Field for Molecular Dynamics Simulations of Alkaline-Earth Carbonates and Their Aqueous Speciation, *J. Phys. Chem. C*, 2015, **119**(43), 24447–24458.
26 D. Gale, J. Raiteri and P. Duin, ACT van. A reactive force field for aqueous-calcium carbonate systems, *Phys. Chem. Chem. Phys.*, 2011, **13**(37), 16666–16679.
27 M. F. Russo and A. C. T. van Duin, Atomistic-scale simulations of chemical reactions: Bridging from quantum chemistry to engineering, *Nucl. Instrum. Methods Phys. Res., Sect. B*, 2011, **269**(14), 1549–1554.
28 G. L. Song and A. Atrens, Corrosion Mechanisms of Magnesium Alloys, *Adv. Eng. Mater.*, 1999, **1**(1), 11–33.
29 A. K. Rappe and W. A. Goddard, Charge equilibration for molecular dynamics simulations, *J. Phys. Chem.*, 1991, **95**(8), 3358–3363.
30 A. Nakano, Parallel multilevel preconditioned conjugate-gradient approach to variable-charge molecular dynamics, *Comput. Phys. Commun.*, 1997, **104**(1), 59–69.
31 H. M. Aktulga, J. C. Fogarty, S. A. Pandit and A. Y. Grama, Parallel reactive molecular dynamics: Numerical methods and algorithmic techniques, *Parallel Comput.*, 2012, **38**(4), 245–259.
32 W. Mortier, S. K. Ghosh and S. Shankar, Electronegativity Equalization Methods for the Calculation of Atomic Charges in Molecules, *J. Am. Chem. Soc.*, 1986, **108**(15), 4315–4320.
33 P. Vajeeston, P. Ravindran, A. Kjekshus and H. Fjellvåg, Pressure-Induced Structural Transitions in MgH_2, *Phys. Rev. Lett.*, 2002, **89**(17), 175506.
34 P. Karen, A. Kjekshus, Q. Huang and V. L. Karen, The crystal structure of magnesium dicarbide, *J. Alloys Compd.*, 1999, **282**(1), 72–75.
35 X. Xia, D. J. Weidner and H. Zhao, Equation of state of brucite; single-crystal Brillouin spectroscopy study and polycrystalline pressure-volume-temperature measurement, *Am. Mineral.*, 1998, **83**(1–2), 68–74.
36 F. Zigan and R. Rothbauer, Neutronenbeugungsmessungen am brucit, *Neues Jahrb. Mineral., Monatsh.*, 1967, **1967**, 137–143.
37 S. Sasaki, K. Fujino and Y. Takéuchi, X-Ray Determination of Electron-Density Distributions in Oxides, MgO, MnO, CoO, and NiO, and Atomic Scattering Factors of their Constituent Atoms, *Proc. Jpn. Acad., Ser. B*, 1979, **55**(2), 43–48.
38 N. L. Ross, The equation of state and high-pressure behavior of magnesite, *Am. Mineral.*, 2015, **82**(7–8), 682–688.
39 M. Catti, A. Pavese, R. Dovesi and V. R. Saunders, Static lattice and electron properties of MgCO3(magnesite) calculated by ab initio periodic Hartree-Fock methods, *Phys. Rev. B: Condens. Matter Mater. Phys.*, 1993, **47**(15), 9189–9198.
40 G. D. Markham, J. P. Glusker, C. L. Bock, M. Trachtman and C. W. Bock, Hydration Energies of Divalent Beryllium and Magnesium Ions: An ab Initio Molecular Orbital Study, *J. Phys. Chem.*, 1996, **100**(9), 3488–3497.
41 M. J. Frisch, G. W. Trucks, H. B. Schlegel, G. E. Scuseria, M. A. Robb and J. R. Cheeseman, *et al.*, *Gaussian 16. Revis A.*, 2016, 3.
42 A. D. Becke, Density-functional thermochemistry. III. The role of exact exchange, *J. Chem. Phys.*, 1993, **98**(7), 5648–5652.

43 C. Lee, W. Yang and R. G. Parr, Development of the Colle-Salvetti correlation-energy formula into a functional of the electron density, *Phys. Rev. B: Condens. Matter Mater. Phys.*, 1988, **37**(2), 785–789.
44 X. Li and M. J. Frisch, Energy-Represented Direct Inversion in the Iterative Subspace within a Hybrid Geometry Optimization Method, *J. Chem. Theory Comput.*, 2006, **2**(3), 835–839.
45 M. Krack and A. M. Köster, An adaptive numerical integrator for molecular integrals, *J. Chem. Phys.*, 1998, **108**(8), 3226–3234.
46 S. Grimme, J. Antony, S. Ehrlich and H. Krieg, A consistent and accurate ab initio parametrization of density functional dispersion correction (DFT-D) for the 94 elements H-Pu, *J. Chem. Phys.*, 2010, **132**, 154104.
47 S. Grimme, S. Ehrlich and L. Goerigk, Effect of the damping function in dispersion corrected density functional theory, *J. Comput. Chem.*, 2011, **32**(7), 1456–1465.
48 J. Furthmüller and G. Kresse, Efficient iterative schemes for ab initio total-energy calculations using a plane-wave basis set, *Phys. Rev. B: Condens. Matter Mater. Phys.*, 1996, **54**(16), 11169–11186.
49 G. Kresse and D. Joubert, From ultrasoft pseudopotentials to the projector augmented-wave method, *Phys. Rev. B: Condens. Matter Mater. Phys.*, 1999, **59**(3), 1758–1775.
50 J. P. Perdew, K. Burke and M. Ernzerhof, Generalized Gradient Approximation Made Simple, *Phys. Rev. Lett.*, 1996, **77**(18), 3865–3868.
51 K. S. Thanthiriwatte, E. G. Hohenstein, L. A. Burns and C. D. Sherrill, Assessment of the Performance of DFT and DFT-D Methods for Describing Distance Dependence of Hydrogen-Bonded Interactions, *J. Chem. Theory Comput.*, 2011, **7**(1), 88–96.
52 E. Torres and G. A. A. DiLabio, Nearly) Universally Applicable Method for Modeling Noncovalent Interactions Using B3LYP, *J. Phys. Chem. Lett.*, 2012, **3**(13), 1738–1744.
53 E. Duboué-Dijon, P. E. Mason, H. E. Fischer and P. Jungwirth, Hydration and Ion Pairing in Aqueous Mg2+ and Zn2+ Solutions: Force-Field Description Aided by Neutron Scattering Experiments and Ab Initio Molecular Dynamics Simulations, *J. Phys. Chem. B*, 2018, **122**(13), 3296–3306.
54 S. Kerisit and S. C. Parker, Free Energy of Adsorption of Water and Metal Ions on the $\{10\bar{1}4\}$ Calcite Surface, *J. Am. Chem. Soc.*, 2004, **126**(32), 10152–10161.
55 M. Galib, M. D. Baer, L. B. Skinner, C. J. Mundy, T. Huthwelker and G. K. Schenter, *et al.*, Revisiting the hydration structure of aqueous Na, *J. Chem. Phys.*, 2017, **146**(8), 084504.
56 M. G. Brik, First-principles calculations of structural, electronic, optical and elastic properties of magnesite MgCO3 and calcite CaCO3, *Phys. B*, 2011, **406**(4), 1004–1012.
57 R. J. Reeder and S. A. Markgraf, High-temperature crystal chemistry of dolomite, *Am. Mineral.*, 1986, **71**(5–6), 795–804.
58 N. L. Ross and R. J. Reeder, High-pressure structural study of dolomite and ankerite, *Am. Mineral.*, 1992, **77**(3–4), 412–421.
59 P.-F. Chen, L.-Y. Chiao, P. Huang, Y. Yang and L. Liu, Elasticity of magnesite and dolomite from a genetic algorithm for inverting Brillouin spectroscopy measurements, *Phys. Earth Planet. Inter.*, 2006, **155**(1), 73–86.
60 B. P. McGrail, H. T. Schaef, V.-A. Glezakou, L. X. Dang and A. T. Owen, Water reactivity in the liquid and supercritical CO2 phase: Has half the story been neglected?, *Energy Procedia*, 2009, **1**(1), 3415–3419.
61 N. Eliaz and E. Gileadi, *Physical Electrochemistry: Fundamentals, Techniques, and Applications*, John Wiley & Sons, 2019, p. 480.
62 H. E. King, M. Stimpfl, P. Deymier, M. J. Drake, C. R. A. Catlow and A. Putnis, *et al.*, Computer simulations of water interactions with low-coordinated forsterite surface sites: Implications for the origin of water in the inner solar system, *Earth Planet. Sci. Lett.*, 2010, **300**(1), 11–18.
63 A. Asaduzzaman, K. Muralidharan and J. Ganguly, Incorporation of water into olivine during nebular condensation: Insights from density functional theory and thermodynamics, and implications for phyllosilicate formation and terrestrial water inventory, *Meteorit. Planet. Sci.*, 2015, **50**(4), 578–589.
64 N. H. de Leeuw, S. C. Parker, C. R. A. Catlow and G. D. Price, Modelling the effect of water on the surface structure and stability of forsterite, *Phys. Chem. Miner.*, 2000, **27**(5), 332–341.
65 O. S. Pokrovsky, J. Schott and F. Thomas, Processes at the magnesium-bearing carbonates/solution interface. I. a surface speciation model for magnesite, *Geochim. Cosmochim. Acta*, 1999, **63**(6), 863–880.
66 S. Kerisit, E. J. Bylaska and A. R. Felmy, Water and carbon dioxide adsorption at olivine surfaces, *Chem. Geol.*, 2013, **359**, 81–89.
67 O. S. Pokrovsky and J. Schott, Processes at the magnesium-bearing carbonates/solution interface. II. kinetics and mechanism of magnesite dissolution, *Geochim. Cosmochim. Acta*, 1999, **63**(6), 881–897.
68 K. Wright, R. T. Cygan and B. Slater, Structure of the (1014) surfaces of calcite, dolomite and magnesite under wet and dry conditions, *Phys. Chem. Chem. Phys.*, 2001, **3**(5), 839–844.
69 A. Michalkova, M. Ilchenko, L. Gorb and J. Leszczynski, Theoretical Study of the Adsorption and Decomposition of Sarin on Magnesium Oxide, *J. Phys. Chem. B*, 2004, **108**(17), 5294–5303.
70 P. Hewlett and M. Liska, *Lea's Chemistry of Cement and Concrete*, Butterworth-Heinemann, 2019, p. 898.
71 K. Jug, B. Heidberg and T. Bredow, Cyclic Cluster Study on the Formation of Brucite from Periclase and Water, *J. Phys. Chem. C*, 2007, **111**(35), 13103–13108.
72 J. Yeon and A. C. T. van Duin, ReaxFF Molecular Dynamics Simulations of Hydroxylation Kinetics for Amorphous and Nano-Silica Structure, and Its Relations with Atomic Strain Energy, *J. Phys. Chem. C*, 2016, **120**(1), 305–317.
73 W. Zhang and A. C. T. van Duin, Second-Generation ReaxFF Water Force Field: Improvements in the Description

of Water Density and OH-Anion Diffusion, *J. Phys. Chem. B*, 2017, **121**(24), 6021–6032.

74 M. Ončák, R. Włodarczyk and J. Sauer, Water on the MgO(001) Surface: Surface Reconstruction and Ion Solvation, *J. Phys. Chem. Lett.*, 2015, **6**(12), 2310–2314, DOI: 10.1021/acs.jpclett.5b00885Available from:.

75 I. V. Markov, *Crystal Growth for Beginners: Fundamentals of Nucleation, Crystal Growth and Epitaxy [Internet]*. 2nd edn, World Scientific, 2003, [cited 2021 May 10]. Available from: https://www.worldscientific.com/worldscibooks/10.1142/5172.

76 S. T. Mergelsberg, S. N. Kerisit, E. S. Ilton, O. Qafoku, C. J. Thompson and J. S. Loring, Low temperature and limited water activity reveal a pathway to magnesite via amorphous magnesium carbonate, *Chem. Commun.*, 2020, **56**(81), 12154–12157.

77 G. D. Saldi, G. Jordan, J. Schott and E. H. Oelkers, Magnesite growth rates as a function of temperature and saturation state, *Geochim. Cosmochim. Acta*, 2009, **73**(19), 5646–5657.

78 E. Wieland, B. Wehrli and W. Stumm, The coordination chemistry of weathering: III. A generalization on the dissolution rates of minerals, *Geochim. Cosmochim. Acta*, 1988, **52**(8), 1969–1981.

79 A. Stefánsson, K. H. Lemke, P. Bénézeth and J. Schott, Magnesium bicarbonate and carbonate interactions in aqueous solutions: An infrared spectroscopic and quantum chemical study, *Geochim. Cosmochim. Acta*, 2017, **198**, 271–284.

80 D. Di Tommaso and N. H. De Leeuw, First Principles Simulations of the Structural and Dynamical Properties of Hydrated Metal Ions Me^{2+} and Solvated Metal Carbonates (Me = Ca, Mg, and Sr), *Cryst. Growth Des.*, 2010, **2010**, 4292–4302.

81 R. M. Siebert and P. B. Hostetler, The stability of the magnesium carbonate ion pair from 10 degrees to 90 degrees C, *Am. J. Sci.*, 1977, **277**(6), 716–734.

82 O. Hoegh-Guldberg, P. J. Mumby, A. J. Hooten, R. S. Steneck, P. Greenfield and E. Gomez, *et al.*, Coral Reefs Under Rapid Climate Change and Ocean Acidification, *Science*, 2007, **318**(5857), 1737–1742.

83 K. S. Lackner, Carbonate Chemistry for Sequestering Fossil Carbon, *Annu. Rev. Energy*, 2002, **27**(1), 193–232.

84 O. Hitoshi and R. Tamas, Structure and dynamics of hydrated ions, *Chem. Rev.*, 1993, **93**(3), 1157–1204.

85 S. Obst and H. Bradaczek, Molecular Dynamics Study of the Structure and Dynamics of the Hydration Shell of Alkaline and Alkaline-Earth Metal Cations, *J. Phys. Chem.*, 1996, **100**(39), 15677–15687.

86 R. K. Lam, A. H. England, A. T. Sheardy, O. Shih, J. W. Smith and A. M. Rizzuto, *et al.*, The hydration structure of aqueous carbonic acid from X-ray absorption spectroscopy, *Chem. Phys. Lett.*, 2014, **614**, 282–286.

87 P. P. Kumar, A. G. Kalinichev and R. J. Kirkpatrick, Hydrogen-Bonding Structure and Dynamics of Aqueous Carbonate Species from Car–Parrinello Molecular Dynamics Simulations, *J. Phys. Chem. B*, 2009, **113**(3), 794–802.

88 F. Bruneval, D. Donadio and M. Parrinello, Molecular Dynamics Study of the Solvation of Calcium Carbonate in Water, *J. Phys. Chem. B*, 2007, **111**(42), 12219–12227.

89 A. Entezari Zarandi, F. Larachi, G. Beaudoin, B. Plante and M. Sciortino, Multivariate study of the dynamics of CO2 reaction with brucite-rich ultramafic mine tailings, *Int. J. Greenhouse Gas Control*, 2016, **52**, 110–119.

90 A. L. Harrison, I. M. Power and G. M. Dipple, Accelerated Carbonation of Brucite in Mine Tailings for Carbon Sequestration, *Environ. Sci. Technol.*, 2013, **47**(1), 126–134.

91 G. Tocci and A. Michaelides, Solvent-Induced Proton Hopping at a Water–Oxide Interface, *J. Phys. Chem. Lett.*, 2014, **5**(3), 474–480.

92 M. F. C. Andrade, H.-Y. Ko, L. Zhang, R. Car and A. Selloni, Free energy of proton transfer at the water–TiO2 interface from ab initio deep potential molecular dynamics, *Chem. Sci.*, 2020, **11**(9), 2335–2341.

93 L. R. Merte, G. Peng, R. Bechstein, F. Rieboldt, C. A. Farberow and L. C. Grabow, *et al.*, Water-Mediated Proton Hopping on an Iron Oxide, *Surf. Sci.*, 2012, **336**(6083), 889–893.

94 S. Wendt, J. Matthiesen, R. Schaub, E. K. Vestergaard, E. Lægsgaard and F. Besenbacher, *et al.*, Formation and Splitting of Paired Hydroxyl Groups on Reduced TiO_2(110), *Phys. Rev. Lett.*, 2006, **96**(6), 066107.

95 J. Comtet, B. Grosjean, E. Glushkov, A. Avsar, K. Watanabe and T. Taniguchi, *et al.*, Direct observation of water-mediated single-proton transport between hBN surface defects, *Nat. Nanotechnol.*, 2020, **15**(7), 598–604.

96 J. Comtet, A. Rayabharam, E. Glushkov, M. Zhang, A. Ahmet and K. Watanabe, *et al.* Anomalous interfacial dynamics of single proton charges in binary aqueous solutions. ArXiv210100231 Cond-Mat [Internet]. 2021; Available from: http://arxiv.org/abs/2101.00231.

97 D. Marx, A. Chandra and M. E. Tuckerman, Aqueous Basic Solutions: Hydroxide Solvation, Structural Diffusion, and Comparison to the Hydrated Proton, *Chem. Rev.*, 2010, **110**(4), 2174–2216.

98 D. Riccardi, P. König, X. Prat-Resina, H. Yu, M. Elstner and T. Frauenheim, *et al.*, ''Proton Holes'' in Long-Range Proton Transfer Reactions in Solution and Enzymes: A Theoretical Analysis, *J. Am. Chem. Soc.*, 2006, **128**(50), 16302–16311.

99 D. Riccardi, P. König, H. Guo and Q. Cui, Proton Transfer in Carbonic Anhydrase Is Controlled by Electrostatics Rather than the Orientation of the Acceptor, *Biochemistry*, 2008, **47**(8), 2369–2378.

100 G. A. Tribello, M. Bonomi, D. Branduardi, C. Camilloni and G. Bussi, PLUMED 2: New feathers for an old bird, *Comput. Phys. Commun.*, 2014, **185**(2), 604–613.

101 S. Kumar, J. M. Rosenberg, D. Bouzida, R. H. Swendsen and P. A. Kollman, THE weighted histogram analysis method for free-energy calculations on biomolecules. I. The method, *J. Comput. Chem.*, 1992, **13**(8), 1011–1021.